Uranium sorption to organic matter and long-term accumulation in a pristine alpine wetland

Pierre Lefebvre, Pierre Le Pape, Arnaud Mangeret, Alkiviadis Gourgiotis, Pierre Sabatier, Pascale Louvat, Olivier Diez, Olivier Mathon, Myrtille O.J.Y. Hunault, Camille Baya, et al.

To cite this version:

Pierre Lefebvre, Pierre Le Pape, Arnaud Mangeret, Alkiviadis Gourgiotis, Pierre Sabatier, et al.. Uranium sorption to organic matter and long-term accumulation in a pristine alpine wetland. Geochimica et Cosmochimica Acta, 2022, 338, pp.322-346. 10.1016/j.gca.2022.10.018 . hal-03855535

HAL Id: hal-03855535
https://hal.science/hal-03855535v1

Submitted on 16 Nov 2022

Uranium sorption to organic matter and long-term accumulation in a pristine alpine wetland

Pierre Lefebvre*[a,χ], Pierre Le Pape[a], Arnaud Mangeret[b], Alkiviadis Gourgiotis[b], Pierre Sabatier[c], Pascale Louvat[d,λ], Olivier Diez[b], Olivier Mathon[e], Myrtille O.J.Y. Hunault[f], Camille Baya[a], Louise Darricau[b], Charlotte Cazala[b,γ], John R. Bargar[g,σ], Jérôme Gaillardet[d], Guillaume Morin[a]

a. Institut de Minéralogie, de Physique des Matériaux et de Cosmochimie (IMPMC), UMR 7590 CNRS-Sorbonne Université-MNHN-IRD, Paris, France
b. Institut de Radioprotection et de Sûreté Nucléaire (IRSN), PSE-ENV SEDRE, Fontenay-aux-Roses, France
c. Université Grenoble Alpes-Université Savoie Mont Blanc-CNRS-EDYTEM, UMR 5204, Le Bourget-Du-Lac, France
d. Université de Paris-Institut de Physique du Globe de Paris-CNRS, UMR 7154, Paris, France
e. ESRF, The European Synchrotron, Grenoble, France
f. Synchrotron SOLEIL, Saint-Aubin, Gif-sur-Yvette, France
g. Stanford Synchrotron Radiation Lightsource (SSRL), SLAC National Accelerator Laboratory, Menlo Park, CA, USA

New addresses:

χ. Soil Chemistry Group, Institute of Biogeochemistry and Pollutant Dynamics, Department of Environmental Systems Science, ETH Zürich, Zürich, Switzerland

λ. Université de Pau et des Pays de l'Adour, E2S UPPA, CNRS, IPREM, Pau, France

γ. Service d'Etude du Comportement des Radionucléides, CEA, Université Paris Saclay, 91190 Gif-sur-Yvette, France

σ. Environmental Molecular Sciences Laboratory, Pacific Northwest National Laboratory, Richland, WA, USA

3rd revised version

Submitted to Geochimica et Cosmochimica Acta

*Corresponding author: Pierre Lefebvre, pierre.lefebvre@sorbonne-universite.fr

ABSTRACT

Understanding the controls on uranium (U) mobility in the environment is key to improve the management of sites contaminated by U mining activities. Previous research has shown that natural or engineered wetlands are particularly able to scavenge high amounts of U(VI) and U(IV) under noncrystalline forms. However, questions remain on the respective roles of sorption and reduction processes in the removal of U from running waters in wetlands, as well as on the long-term stability of U storage. Here, we performed a series of geochemical, isotopic (δ^{238}U, (^{234}U/^{238}U)), microscopic (SEM-EDXS, EPMA) and spectroscopic (µ-XRF, µ-XAS, XANES and EXAFS at the U L_3 and M_4-edges and Fe K-edge) investigations to determine the modes of U accumulation and assess U mobility in a natural exceptionally U-enriched (up to 5000 µg/g) wetland on the shore of Lake Nègre (Mediterranean Alps, France). Uranium (VI) was largely dominant in the two studied soil cores, except a few samples containing as much as ~50 % U(IV). At the particle scale, U is associated to a variety of organic constituents of the soil matrix with a homogenous oxidation state. Bulk EXAFS spectroscopy at the U L_3-edge shows that U is mostly mononuclear, with dominant monodentate binding to organic moieties (C neighbors at ~3.45 Å). An additional minor fraction of U under polymeric forms is inferred from wavelet (CCWT) analysis of the EXAFS data. These observations are reinforced by 1 M bicarbonate extractions that result in the dissolution of 82-96 % of total U, including putative polymeric species. At the wetland scale, similar or slightly fractionated isotopic ratios (δ^{238}U) between the wetland-feeding creek waters and the wetland soils are observed, supporting the idea that U(VI) sorption on organic matter is the primary U scavenging mechanism. Furthermore, it indicates that partial U(VI) reduction to U(IV) occurs as a second step, after sorption. Analysis of U decay chain disequilibria in the cores as a function of depth suggests that U accumulation in this wetland has lasted for several thousand years. We propose that the wetland acts as an active reactor where U has been massively accumulating for ~14500 years, especially as U(VI) forms associated to organic matter, and is further partly exported to the lake through soil erosion.

KEYWORDS

Noncrystalline Uranium; Wetland; Uranium speciation; Uranium isotopes; U(VI) polymeric species

1. INTRODUCTION

Past uranium (U) mining activities have raised worldwide environmental, health, remediation and long-term management concerns (Abdelouas, 2006; Newsome et al., 2014), including in France (GEP, 2010; IRSN, 2019). As part of the global strategy to improve the management of U-contaminated sites, particularly to strengthen the projections on the short- and long-term U behavior, it is critical to understand the factors controlling the speciation and mobility of U in natural environments (e.g., Regenspurg et al., 2010; Campbell et al., 2012; Wang et al., 2013; Morin et al., 2016; Mikutta et al., 2016; Gourgiotis et al., 2020). In that context, the Lake Nègre catchment in the Mercantour-Argentera massif (Mediterranean Alps, South-East France) appears as a natural analogue of contaminated sites since exceptionally high U concentrations of natural origin were observed in the lake sediments and in the watershed streams (AERMC, 2008; Lefebvre et al., 2021a, b). In this pristine environment, the processes involving U species can be observed at several scales of time and space. In the long term, U speciation provided important clues about climatic and mineralogical controls on the sources, composition and diagenetic fate of U in the lake sediments since the last deglaciation (Lefebvre et al., 2021a, b). These previous studies referred to the potential role of the wetland located right upstream of Lake Nègre, along with the watershed soils, in controlling U inputs to the lake through U scavenging by organic matter (OM) followed by U export to the lake through soil erosion (Lefebvre et al., 2021b).

Uranium accumulation in wetlands has been well documented (e.g., Owen and Otton, 1995) and several studies over the past decade have contributed to improve our understanding of micro-scale processes responsible for U scavenging (Regenspurg et al., 2010; Wang et al., 2013, 2014; Li et al., 2015; Mikutta et al., 2016; Stetten et al., 2018a, 2020; Fuller et al., 2020; Le Pape et al., 2020). A main underlying objective of these studies was to evaluate the potential of artificial wetlands to attenuate U release from highly contaminated sites such as mine tailings (e.g., Schöner et al., 2009; Fuller et al., 2020). In pristine environments, U usually originates from the leaching of a U-rich igneous source rock (e.g., Regenspurg et al., 2010; Fuller et al., 2020) and is subsequently trapped downstream by the soil OM. In organic-rich soils, U accumulation can reach several thousand parts per million (µg/g) in both its oxidized (U(VI)) and reduced (U(IV)) states. The U(VI) form is usually dominating, in particular as noncrystalline (also known as mononuclear) species bound to organic moieties (Regenspurg et al., 2010; Mikutta et al., 2016; Fuller et al., 2020). Similar observations were made in U mining-contaminated wetlands with even higher U accumulation, primarily originating from mine waste piles but also locally from redistribution from U particles-rich discharge layers (Schöner et al., 2009; Wang et al., 2013, 2014; Mangeret et al., 2018; Stetten et al., 2018a, 2020; Gourgiotis et al., 2020; Le Pape et al., 2020; Martin et al., 2020; Kaplan et al., 2020).

In wetland soils, high U accumulation is enhanced by elevated organic matter content, which provides abundant U binding sites and boosts microbial activity. Microbial respiration in such water-saturated media then potentially generates reducing conditions, favoring U(VI) reduction to less soluble U(IV) species (Maher et al., 2013). Uranium partitioning in the solid phase may occur through complexation of U(VI) and U(IV) to organic moieties, and, to a lesser extent, sorption to mineral surfaces (Regenspurg et al., 2010; Mikutta et al., 2016; Bone et al., 2017b, 2020; Stetten et al., 2018a; Fuller et al., 2020) and/or through precipitation of U(IV) or U(VI) mineral species, as evidenced for instance in organic-rich lenses in alluvial sediments (Noël et al., 2017, 2019). Uranium mobility is then driven by the solubility of solid U species, in other words by the solid-phase U speciation. In that respect, noncrystalline U species have raised attention over the past decade because of their higher sensitivity to redox cycling and dissolution (e.g., Cerrato et al., 2013; Seder-Colomina et al., 2018; Newsome et al., 2015 and references therein). Additionally, questions remain about the long-term evolution of mononuclear U species in soils subject to redox fluctuations, as is often the case for wetland soils.

Several questions remain unsolved regarding the exact mechanisms leading to both U(IV) and U(VI) fixation by wetland soil OM. Among these, the relative importance of sorption and microbially-mediated reduction and the timing of both reactions need to be further investigated (Mikutta et al., 2016). The observation of significant U(IV) proportions in soils may indeed be attributed either to reduction of aqueous U(VI) followed by U(IV) incorporation in the solid phase (Noël et al., 2017, 2019), or to the reduction of already-bound U(VI), as proposed for instance by Stetten et al. (2018a, 2020) in a contaminated wetland. The reaction sequence may impact the composition of U solid products and consequently U mobility. Deciphering between both processes requires a selective proxy, such as the $^{238}U/^{235}U$ isotope ratio (expressed as $\delta^{238}U$), which has been shown to discriminate between reduction and adsorption (Andersen et al., 2017 and references therein). In this framework, the use of this proxy could be strengthened by the determination of the U oxidation state and speciation, notably in a direct way *via* X-Ray Absorption Spectroscopy (XAS). Such an approach may help to determine whether the formation of mononuclear U(IV) solid species in wetland soils primarily results from the reduction of aqueous U(VI) species and subsequent sorption of U(IV) and/or if the affinity of U(VI) for organic moieties leads to efficient U(VI) sorption and further reduction into mononuclear U(IV).

In this perspective, better determining whether U(VI) to U(IV) reduction remains a prerequisite for U scavenging in wetlands may help to better assess the capacity of various types of wetlands to accumulate U as a function of hydrological conditions and geological settings. Moreover, evaluating the necessity to maintain reducing conditions in the long term to immobilize uranium may be useful to improve contaminated soils management strategies, and to optimize natural remediation processes.

To that purpose, we combined a series of complementary analyses including U isotope ratios ($\delta^{238}U$ and ($^{234}U/^{238}U$)), gamma spectrometry, micro-and meso-scale U solid state redox and speciation data (determined by (μ-)XAS) along with micro-X-Ray Fluorescence (μ-XRF), scanning electron microscopy (SEM-EDXS) and electron microprobe (EPMA) analyses on two pedologically distinct cores from the Lake Nègre wetland. We show that the wetland accumulated massive amounts of U (up to > 5000 μg/g) and we discuss (i) the molecular-scale mechanisms responsible for such a remarkable enrichment and (ii) the U redox and sorption dynamics in this waterlogged soil over a several thousand years period.

2. MATERIALS AND METHODS

2.1. Study site and sampling

2.1.1. Soil cores sampling

Lake Nègre is located at the outlet of a high-altitude catchment (alt. 2356 m) with scarce alpine meadows covering a granitic bedrock, as described in Lefebvre et al. (2021a, b). The wetland studied here is located on a flat area north of the lake where two creeks meander on the eastern and western sides of the wetland before flowing into the lake (Figure 1). The organic-rich, non-peaty waterlogged soils of the wetland (that might be compared to sediments, see Discussion section 4.1.1) are covered by herbaceous plants and are variably water-saturated. In September 2018, two soil cores of 30 cm (NEG18-ZH1-C1 and -C2) were sampled by push coring (PVC tubes, 50 mm diameter) down to the bedrock and immediately conditioned into sealed aluminized plastic bags purged with N_2 (Figure S1). Core C1 was sampled in a flooded area covered with stagnant water; core C2 was collected in a dry creek bed and was partially water-saturated (water level 5 cm below ground surface). Both cores are located on the eastern side of the wetland, downstream of a discontinuous stream which flows partially underground and is presumed to resurge in the cores sampling area (Figure 1). The cores were transported and stored at ~4 °C before being opened at the laboratory in a COY anaerobic glovebox ($O_2 <$ 20 ppm) and cut into 2 cm slices (except C2 between 24 and 30cm: one sample). These slices were cut into two halves: one half was vacuum-dried and stored in sealed vials inside the glovebox for further analyses; the second half was dried in open air at 30 °C in an oven for gamma spectrometry. Chemical, isotopic and radiochemical analyses were conducted in open air, whereas bicarbonate extractions (section 2.4) and micro/bulk X-ray absorption spectroscopy analyses (section 2.5) were performed in anoxic atmospheres.

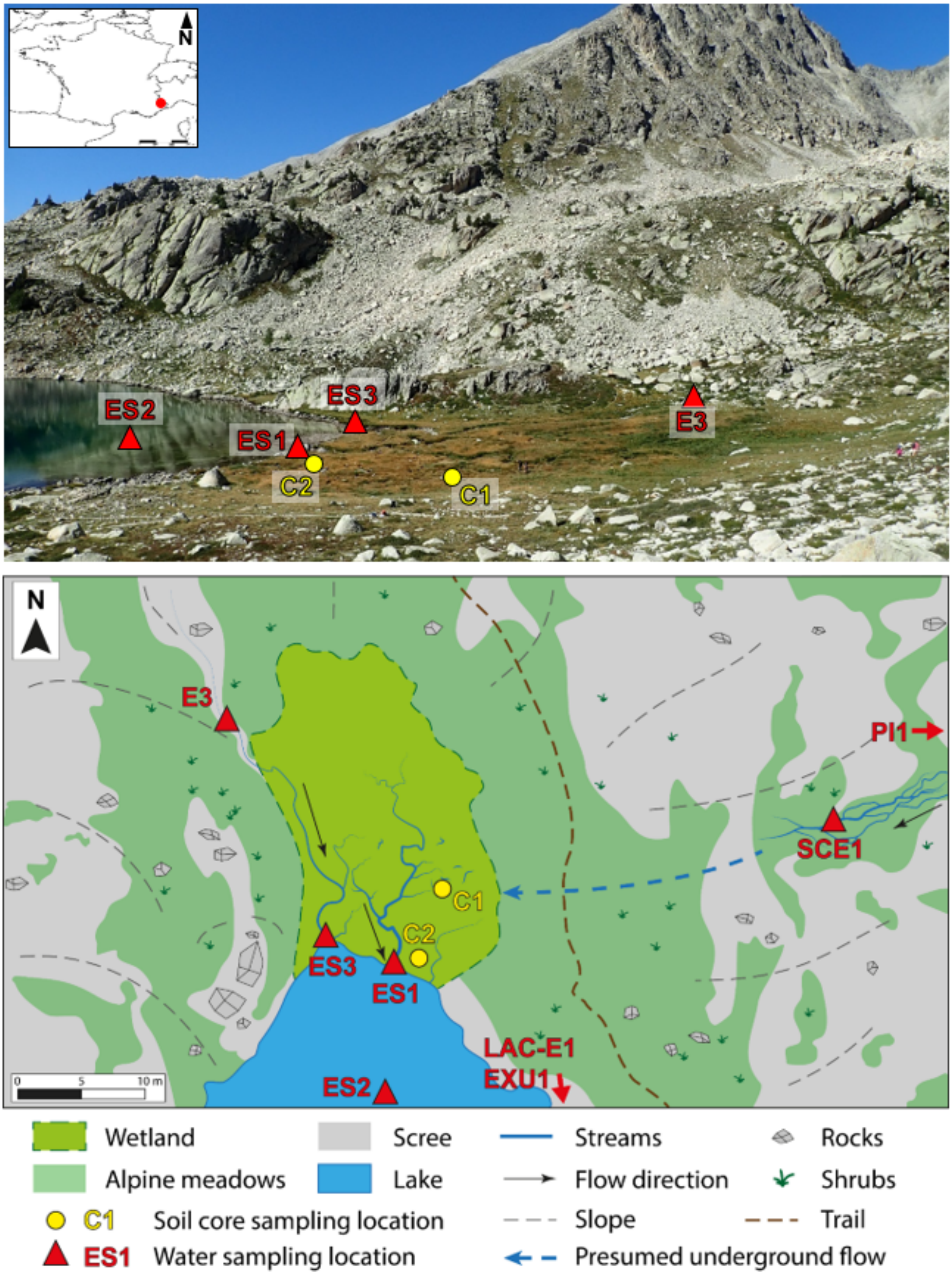

Figure 1 – Sampling locations in the studied wetland upstream of Lake Nègre. *(Top) Soil cores (yellow circles) and water (red triangles) sampling points located in a photograph taken from point SCE1); (Bottom) Sketch map of the wetland system with sampling locations. (Photograph courtesy of P. Blanchart, IRSN).*

2.1.2. Stream waters sampling

In September 2019, we collected stream waters upstream of the wetland and downstream where the creeks flow into the lake (Figure 1). In the eastern creek, we collected water at the spring, downhill of a large scree (PI1), then downstream in the slope overlooking the wetland where the stream is braided over a vegetation-covered soil (SCE1). This stream then disappears and flows underground, probably feeding on a large scale the east side of the wetland where cores C1 and C2 were sampled. Sampling point ES1, at the outlet of the eastern stream crossing the wetland, is therefore thought to be hydrologically connected to PI1 and SCE1. The ES2 sampling point is located in the lake ~20 m downstream of ES1, at the south end of a flat shallow platform where abundant vegetal particles settled on the lake bottom (roughly visible in Figure 1). We also sampled waters up- (E3) and downstream (ES3) of the wetland in the western stream, as well as on the eastern shore of the lake ~100 m from the wetland (LAC-E1) and in the lake outlet stream (EXU1).

At three locations up- and downstream of the east side of the wetland (SCE1, ES1, ES2), the waters were vacuum-filtered in the field at 0.2 µm (nitrocellulose filters – GSWP) with a Sartorius filtration unit and subsequently ultrafiltered under positive pressure at 100 kDa with an Amicon cell equipped with regenerated cellulose ultrafiltration disks. Additional (ultra)filtration steps were done but not retained here: a 0.01 µm filtration because of a filter size similar to 100 kDa, and a 1 kDa ultrafiltration which results are not reliable because of potential U retention by the membrane (Guo et al., 2007). Filtration results at point ES2 were already described in Lefebvre et al. (2021a). At other sites (PI1, E3, ES3, LAC-E1 and EXU1), a single 0.2 µm filtration step was used. The filtration units and sample vials were washed beforehand with nitric acid (HNO_3 0.1 N). Filtration blanks were realized in the field with ultrapure (milliQ) water. All samples were acidified with distilled (ultrapure) HNO_3 after subsampling aliquots for anions and dissolved organic carbon (DOC) measurements and stored at 4 °C before analysis. The physicochemical parameters (pH, temperature T, oxidation reduction potential ORP, dissolved O_2, conductivity σ) of all sampled waters except LAC-E1 and EXU1 were measured onsite at the time of sampling with field WTW 350i and 3420 multi-parameter probes. The redox potential (ORP) was measured with a WTW Sentix ORP platinum-Ag/AgCl electrode. During the same field trip, i.e., one year after sampling the soil cores, we measured the depth profile of the same parameters at the sampling locations of cores C1 and C2 (see *Supplementary Material* page 8).

2.2. Chemical and mineralogical analyses

2.2.1. Chemical and radiochemical analyses

Unless stated otherwise, most chemical analysis protocols used in this study are reported in Lefebvre et al. (2021a). Briefly, a selection of soil samples was ground, sieved (~500 µm) and digested with a mix of HNO_3, HF and $HClO_4$. Major, minor and trace elements of soils and waters were analyzed by optical and mass spectrometry with a ThermoFisher ICAP 7600 DUO ICP-AES and an Agilent 8800 ICP-MS/MS at the LUTECE laboratory (IRSN). Major anions in the filtered waters were analyzed by ionic chromatography with a Metrohm 930 Compact IC Flex. Total organic and inorganic carbon (TOC, TIC) were measured with a carbon analyzer (Vario TOC Elementar); TIC was found to be negligible in the acidic soils, located in a carbonate-free watershed. Light elements (C, H, N, S) were also analyzed in the soil samples with a ThermoScientific FlashSmart elemental analyzer; the soil TOC contents given below are average values of the two measurements. Gamma spectrometry measurements of radionuclides (^{238}U (from ^{234}Th), ^{232}Th (from ^{228}Ac), ^{230}Th, ^{226}Ra, ^{210}Pb, ^{137}Cs, ^{40}K) were performed along both cores with a well-type high-purity/low-noise Ge ORTEC GWL Series detector. We also analyzed reference compounds RGU-1, RGTh-1, 131SL300 and 161SL300 (from IRSN), IAEA-312 and 314 (from IAEA) to control the detectors efficiency and background noise. ^{238}U and ^{232}Th activities (in Bq/kg) were converted to mass concentrations (in µg/g) using the specific activity values of 12.44 and 4.06 kBq/g respectively.

Because uranium is much more mobile in surface environments than thorium (Th), the proportion of detrital U $F(U_{detrital})$ in the core soils can be classically estimated from U/Th ($^{238}U/^{232}Th$) ratios, using a simple mixing model where all Th is considered detrital (Equation 1):

$$F(U_{detrital})\ [\%] = \frac{\left(U/_{Th}\right)_{det}}{\left(U/_{Th}\right)_{soil}} \times 100 \qquad (1)$$

Where $(U/Th)_{soil}$ is the measured soil atomic ratio and $(U/Th)_{det}$ is the detrital atomic ratio corresponding to the bedrock of the studied watershed, measured at 0.26 ± 0.13 (Lefebvre et al., 2021a) in agreement with the average Upper Continental Crust value (Rudnick and Gao, 2003). For calculating $F(U_{detrital})$ values, we used U/Th ratios measured by ICP-MS or by gamma spectrometry.

2.2.2. Mineralogical observations and analyses

The bulk mineralogical composition of the soils was determined by powder X-Ray Diffraction (XRD) using the Co K_α radiation over the 4-80° 2θ range with a 0.03° step. Data were collected in continuous scan mode in Bragg-Brentano geometry using a Panalytical Xpert-Pro diffractometer. For SEM observations, sample powders were embedded into a Mecaprex MT1 epoxy resin, polished and carbon coated. A Zeiss Ultra 55 microscope at IMPMC, equipped with a Field Emission Gun (FEG) and a Bruker Si-drift detector for energy-dispersive X-ray spectrometry (EDXS), was used in back-scattered electron mode with a 15 kV emission and at a working distance of 7.5 mm. EDXS micro-analyses were performed as well as EDXS chemical mapping.

The micro-scale chemical composition of a few samples was additionally quantified using a Cameca SX-Five Electron Probe Micro Analyzer (EPMA) equipped with 5 Wavelength-Dispersive Spectrometers (WDS) and an Energy Dispersive Spectrometer (EDS), at the CAMPARIS platform (OSU Ecce Terra). The samples were prepared as for SEM-EDXS with an additional C metallization layer. The EPMA was operated with an accelerating voltage of 15 kV and a beam current of 10 nA. Ten elements (Na, Al, Mg, K, Ca, P, Fe, Si, S, U) calibrated with standard minerals were analyzed on several positions of each observed structure. We targeted U-bearing phases previously observed by SEM along with additional phases. Because of the high organic content of the studied soil samples, the total values of EPMA analyses are well below 100 wt% (10 to 35 wt%). Results are thus expressed only in atomic percentages (at%).

2.3. Isotopic analyses

For the determination of U isotopic ratios ($^{238}U/^{235}U$ and $^{234}U/^{238}U$), digested solids and waters were spiked with a double-tracer (IRMM-3636a) and U fractions were separated on an UTEVA resin column (Eichrom Technologies). The measurements were performed on a Thermo Finnigan Neptune MC-ICP-MS housed at the PARI platform (IPGP). A dual Scott/cyclonic spray chamber with a micro-flow PFA nebulizer (ESI, USA) were used as the introduction system. All isotope signals were collected simultaneously in Faraday cups equipped with 10^{11} Ω (for $^{233, 235, 236, 238}U^+$ and ^{232}Th isotopes) and 10^{13} Ω (for $^{234}U^+$ isotope and the $^{239}Pu^+$ for the estimation of $^{238}UH^+$ formation) feedback resistors. The instrumental settings were optimized before each new analytical session and typical sensitivity for $^{238}U^+$ was ~70 mV / ppb of U. The instrumental mass bias was corrected internally using the exponential mass fraction law (Russell et al., 1978) and the corrected ratios were bracketed with the IRMM-184 certified solution in order to express the $^{238}U/^{235}U$ ratios with the delta notation relative to the more common standard CRM-145 (Equation 2):

$$\delta^{238}U \quad [‰] = \left(\frac{{}^{238}U/{}^{235}U_{sample}}{{}^{238}U/{}^{235}U_{standard}} - 1 \right) \times 1000 \qquad (2)$$

($^{234}U/^{238}U$) activity ratios were obtained by multiplying the $^{234}U/^{238}U$ isotope ratio with the half-life ratio T_{238}/T_{234} of the isotopes. Each sample was analyzed 3-5 times, the uncertainties (2SD) being calculated on all replicates. Reference materials (BCR-2, HU-1, AGV-2, RGU-1) were processed and analyzed along with the samples: their isotopic composition are in good agreement with published data (see Lefebvre et al., 2021a).

2.4. Bicarbonate extractions

In order to quantify the fraction of noncrystalline U, bicarbonate extractions were performed by reacting soils samples with 1 M $NaHCO_3$ for 100 h in an anoxic glovebox using O_2-free water, as described in Lefebvre et al. (2021a) following a protocol adapted from Alessi et al. (2012). After two rinsing steps with O_2-free milliQ water, the solid residues were centrifuged, vacuum-dried, acid-digested and then analyzed for U and Th by ICP-MS. Duplicate extractions were performed on three samples with consistent results. Based on these duplicates, the combined uncertainty (2SD) on bicarbonate-extracted fractions (in % of total U) was 9.0 %.

2.5. X-Ray Absorption Spectroscopy (XAS)

2.5.1. Bulk U L_3-edge XANES and EXAFS data collection and analysis

Bulk soil samples were finely ground in an agate mortar, prepared as Kapton tape-covered pellets and mounted on cryostat multi-sample holders that were shipped to synchrotron facilities in individual air-tight containers to preserve the samples from oxidation. The containers were handled in glove bag or glovebox at the synchrotron beamlines. The sample holder was rapidly screwed on the cryostat rod and immediately inserted in the cryostat sample chamber, and further maintained under purged He atmosphere during the measurements.

A first set of U L_3-edge XAS data was collected in December 2018 at 10 K on the undulator beamline P64 (Deutsches Elektronen-Synchrotron – DESY). Ten bulk wetland soil samples from cores C1 (2-4, 8-10, 14-16, 20-22 and 26-28 cm) and C2 (2-4, 8-10, 14-16, 20-22 and 24-30 cm) were analyzed (this study), as well as the Lake Nègre sediment bulk sample NEG18-07 189-194 cm (Lefebvre et al. 2021a). The beamline incident energy was selected with a Si(111) double crystal monochromator, and the sample fluorescence intensity was measured using a Passivated Implanted Planar Silicon total fluorescence detector. Between 5 and 40 XAS scans were acquired in continuous mode (5.5 min per scan) on each sample. Because of moderate but measurable photo-reduction of U under beam exposure on this high-flux beamline, only the first scan was used for X-Ray Absorption Near-Edge Structure (XANES) analysis. In the same way, only the first scans exhibiting less than 17% of U photo-reduction were merged for extracting Extended X-ray Absorption Fine Structure (EXAFS) data. This value was chosen as a compromise for obtaining reliable signal/noise ratio and maintaining beam-damage effects close to the EXAFS detection limit.

A second set of U L_3-edge XAS data was collected in June 2021 at 10 K on the 2-pole wiggler beamline BM23 (European Synchrotron Radiation Facility – ESRF) in order to obtain higher *k*-range data for the bulk wetland soil samples C1 18-20 cm and C1 20-22 cm (duplicate of P64 measurement). In addition, solid residues obtained after 1 M bicarbonate extraction of samples C1 20-22 cm and C2 2-4 cm, together with the Lake Nègre sediment bulk sample NEG18-07 184-189 cm already analyzed by Lefebvre et al. (2021a) were also analyzed for XANES data. The energy was selected with a Si(111) double-crystal monochromator and the samples were placed in a liquid He cryostat maintained at a temperature of 10 K. XAS measurements were performed in transmission detection mode for the two U-rich soil samples and in fluorescence detection mode with a Vortex silicon-drift energy-dispersive fluorescence detector for the other samples. Between 40 and 121 scans were collected on each sample, in continuous mode at a speed of 6.8 eV/s using a 50 ms sampling time (0.34 eV steps). Variable energy ranges within the XANES to EXAFS region were chosen depending on the samples, which resulted in 2- to 4-min long XAS scans. No beam-damage was observed for any sample under these data collection conditions.

All bulk XAS spectra at the U L_3-edge were merged, normalized and background-subtracted using the Athena software (Ravel and Newville, 2005). The incident beam energy was calibrated by setting to 17,038.0 eV the first inflection point of the yttrium (Y) *K*-edge transmission spectrum acquired on an Y foil using a double-transmission setup. The EXAFS spectra were binned to a 0.04 Å^{-1} *k*-step and deglitched when necessary, and the E_0 value was set to 17173.4 eV, which corresponds to the inflexion point of the U(VI) L_3-edge (e.g., Seder-Colomina et al., 2015). For samples acquired at DESY, we limited the EXAFS energy range to the 17.140-17.965 keV region because of the presence of Y and Zr in our natural samples, which yield X-ray absorption *K*-edges at 17.038 and 17.998 keV, respectively.

U L_3-edge data for a large set of model compounds (Tables S2 and S5) was used to help determining the U redox state and molecular-level speciation in the soil samples studied. Our database contains especially U(VI) and/or U(IV) humate, citrate, pyrophosphate and biosorbed complexes (Seder-Colomina et al., 2015; Morin et al., 2016; Stetten et al., 2018a, 2020), U(VI) sorbed/coprecipitated to/with ferrihydrite or amorphous iron phosphate (Seder-Colomina et al., 2015), U(VI) sorbed to illite and chlorite (Othmane et al., 2013), as well as natural and synthetic U-minerals (Morin et al., 2016; Stetten et al., 2018a; Lefebvre et al., 2021a). Our reference database also includes natural sediment samples NEG18-07 184-189 cm and NEG18-07 189-194 cm from Lake Nègre (Lefebvre et al., 2021a) that are naturally reduced, as well as a reduced U(IV)-humus natural sample (Stetten et al., 2018a, 2020). In the present study our set of model compounds was completed with a U(VI)-citrate complex prepared following a similar method to that used for preparing U(IV)-citrate, as well as U(IV)- and U(IV)-pyrophosphate (Morin et al., 2016). Briefly, U(VI)-citrate was prepared in a Jacomex anoxic glovebox by mixing ~1.5 mL of a 260 mM citric acid O_2-free solution at pH 2 (100 mg sodium citrate in 1.5 mL H_2O + a droplet of 35 wt % HCl), with 0.4 mL of a 2 mM U(VI) nitrate O_2-free solution, and raising the pH of the mixture to 6.5 with an appropriate volume of 1 M NaOH O_2-free solution. The mixed solution was stirred for 1 h and then evaporated under vacuum within the glovebox to obtain U(VI)-citrate as a solid paste with U concentration of about 1.9 wt%.

Least-square linear combination fitting (LCF) of XANES spectra at the U L_3-edge was performed using a Fortran 90 custom-built software based on a Levenberg-Marquardt minimization algorithm, similar to the software used in previous studies from our group (e.g., Seder-Colomina et al., 2015; Morin et al., 2016; Stetten et al., 2018b; Lefebvre et al., 2021a). The fit quality was estimated with a *R*-factor, $R_f = \Sigma[\mu_{exp}-\mu_{fit}]^2 / \Sigma\mu_{exp}^2$, where μ is the normalized absorbance and with a reduced chi-square, $Chi^2_R = N/(N-N_p)\ \Sigma[\mu_{exp}-\mu_{fit}]^2 / \Sigma\mu_{exp}^2$, where N_p is the number of fitting components and *N* is the number of independent parameters corresponding to the energy range divided by the natural width of the U L_3 levels reported by Krause and Oliver (1979). The uncertainty on each fitting parameter *p* was estimated to 99.7% confidence as $3\sqrt{(\mathrm{var}(p).Chi^2_R)}$, where var(*p*) is the variance of parameter *p* returned by the Levenberg–Marquardt routine for the lowest Chi^2_R value.

Prior to LCF analysis of EXAFS data, a Principal Component Analysis (PCA) of the k^3-weighted U L_3-edge EXAFS spectra dataset of our wetland samples was performed over the 2-12 $Å^{-1}$ *k*-range using the SIXpack program (Webb, 2005). The PCA was followed by a Target Transform (TT) analysis of our model compound spectra database in order to select the most relevant components to perform LCF analysis of the wetland samples EXAFS data. Least-square LCF of EXAFS spectra was then performed using a Fortran 90 custom-built software based on a Levenberg-Marquardt minimization algorithm, similar to the software used in previous studies (e.g., Stetten et al., 2018a, 2020). The unfiltered experimental $k^3\chi(k)$ functions were fit in *k*-space over the 2-12 or 2-10 $Å^{-1}$ *k*-range, for the C1 and C2 cores samples, respectively, data being noisier for C2. The fit quality was estimated with a *R*-factor, $R_f = \Sigma[\mu_{exp}-\mu_{fit}]^2 / \Sigma\mu_{exp}^2$, and with a reduced chi-square, Chi^2_R, similar to that used for shell-by-shell fitting described hereafter.

Shell-by-shell fitting of the unfiltered U L_3-edge k^3-weighted EXAFS spectra was performed using a Fortran 90 custom-built least-squares fitting software based on a Levenberg-Marquardt minimizing algorithm, similar to the code used in previous studies (e.g., Seder-Colomina et al., 2015; Morin et al., 2016; Stetten et al., 2018b; Lefebvre et al., 2021a). In this code, the $\chi(k)$

function is calculated with the plane-wave formalism (Teo, 1986), implementing backscattering amplitude and phase functions calculated using the curved-waves theory with the FEFF8.1 code (Ankudinov et al., 1998). Single and multiple backscattering functions were calculated from the crystal structures of torbernite (Locock and Burns, 2003) for U-O (axial and equatorial) and U-P paths, uranyl acetate dehydrate (Howatson et al., 1975) for U-C paths, $CaU(PO_4)_2$ (Dusausoy et al., 1996) for U-P paths, and coffinite (Fuchs and Gebert, 1958) for U-Si and U-U paths.

For both EXAFS LCF and shell-by-shell fitting, the fit quality was estimated by a reduced chi-square parameter Chi^2_R, = $N_{ind}/[(N_{ind}-N_p).n.\varepsilon^2] \sum [k^3\chi(k)_{\mathrm{exp}} - k^3\chi(k)_{\mathrm{calc}}]^{2,}$ with $N_{\mathrm{ind}} = (2\Delta k\Delta R)/\pi$, the number of independent parameters, N_p the number of free fitting parameters, n the number of data points, and ε the root mean square of the data noise. This latter value was estimated as the Fourier back-transform of the data in the 15–25 Å R-range, following a method modified after Ravel and Newville (2005). The uncertainty on EXAFS fitting parameters was estimated by $3.\sqrt{(\mathrm{var}(p).Chi^2_R)}$, where var($p$) is the variance of parameter p returned by the Levenberg-Marquardt routine for the lowest Chi^2_R, value.

Fast Fourier Transforms (FFT) of the k^3-weighted experimental and fit EXAFS spectra were calculated after having applied a Keiser-Bessel window with a Bessel weight of 2.5. Continuous Cauchy Wavelet Transforms (CCWT) of the experimental and fitted EXAFS spectra were calculated using the MATLAB script by Muñoz et al. (2003, 2005). In order to decipher between close fitting solutions, fit quality of the second neighbor contributions were examined in R space (e.g., Wang et al., 2011) by a reduced chi-square parameter $Chi^2_{R\text{-}FFT} = N_{ind}/[(N_{ind}-N_p).n.\varepsilon_r{}^2] \sum [|FFT_{exp}| - |FFT_{calc}|]^2$, within the 1.5-5 Å R-range, with ε_r the root mean square of the data noise in the 15–25 Å R-range. Comparisons of fit solutions were done according to F-tests at 95 or 90 % confidence.

2.5.2. Micro-XRF and U L_3-edge micro-XANES analysis

Micro-X-Ray Fluorescence (μ-XRF) mapping and subsequent μ-XANES analyses of soil sample C1 18-20 cm were conducted at ESRF beamline BM23. Data were collected at room temperature and the X-ray beam was focused with two mirrors in Kirkpatrick–Baez (KB) geometry to a ~3x3 μm^2 full width at half maximum at sample position. An optical microscope focused on sample position was placed right above the beam for proper tracking of the analyzed spot. The sample was embedded in epoxy resin as for SEM observations but within a N_2-filled glove bag to prevent exposure to air, covered with Kapton tape to limit oxidation during the experiment and placed perpendicular to the X-Ray beam. A continuous N_2 flow was applied on the sample surface to prevent oxidation by air over the course of the experiment. The Si-drift fluorescence detector was placed at a 45° angle between the beam and the sample plane.

The incident beam energy was selected using a Si(111) double-crystal monochromator and was set to 17.5 keV for μ-XRF mapping. The emission spectrum energy was calibrated using the Cu K_α and K_β emission lines from Cu tape. The XRF spectra were converted to element-specific fluorescence intensity maps with the PyMca software (Solé et al., 2007) through batch curve fitting of emission lines of elements of interest (including U L_α and Fe K_α). We acquired 2x2 mm^2 μ-XRF maps with horizontal 5 μm steps and vertical 10 μm steps, with a counting time of 0.2 s per point. After μ-XRF mapping, U-rich areas of interest were analyzed for their U oxidation state by μ-XANES at the U L_3-edge. For this purpose, μ-XAS spectra (1000 points, 50 ms/point) were measured from 17.050 to 17.550 keV (17.400 keV for the first spectra), for a total duration of ~66 seconds.

Room-temperature beam-damage kinetics (U(VI) photo-reduction) was estimated by acquiring 7 to 10 successive scans on the same spot, at four different locations (see Figure 7, points *a* to *d*). Each scan was LC fitted to determine the evolution of U(VI) and U(IV) proportions over time (Figures S2 and S3). At all spots, the U(IV) proportion significantly increased over time, ultimately exceeding U(VI) at two spots after 4 to 6 minutes. These kinetic measurements showed that every second scan acquired on the same position was significantly impacted by beam exposure, while the first scan (66 s acquisition time) was always affected by less than 10 % of relative U(VI) reduction. Proper U redox could thus be determined by LCF of μ-XANES spectra obtained by merging individual first scans acquired on pristine spots of a same U-bearing area through successive displacements of > 10 μm between each scan acquisition. To do so, additional μ-XRF map were acquired on selected areas where necessary, with horizontal and vertical 2.5 μm steps to obtain more detailed chemical maps.

These μ-XANES spectra were rebinned, normalized and merged using the Athena software. LC fitting was done with the same code and same U(VI) and U(IV) standards as for bulk XANES spectra. Energy was calibrated once at the start of the beamtime using an Y foil in single transmission mode. Monochromator instability – i.e., the deviation of the incident energy during the course of the experiment – was then accounted for by refining an energy shift parameter for the experimental μ-XANES spectra to properly fit with the mixture of U(VI) and U(IV) reference spectra. The obtained energy shift values consistently showed a regular deviation trend over time.

2.5.3. Bulk U M_4-edge XANES analysis

In order to complement U redox determination by U L_3-edge XANES and document the possible occurrence of U(V) species, we performed U M_4-edge High Energy-Resolution Fluorescence Detected (HERFD)-XANES spectroscopy measurements on the MARS beamline at the SOLEIL synchrotron in July 2020. Five soil samples (3 from core C1 and 2 from core C2) were prepared as thin sample pellets. The measurements were performed at room temperature, in similar conditions as those described in Le Pape et al. (2020). Briefly, the incident beam energy was selected with a double Si(111) crystal monochromator and calibrated by setting the inflection point of the absorption K-edge of potassium from a KBr pellet at 3608 eV. The U M_β emission line was analyzed with a Si(220) crystal analyzer with a curvature radius of 1 m. The measurements were done at the maximum of the M_β emission line at 3336.0 eV. As the experiment was performed at low energy (3.7 keV), we sought to avoid attenuation of the incident and fluorescence-emitted X-rays through absorption by thick Kapton tape and scattering by air. To this end, the sample pellets were sealed with thin 12 µm Kapton tape, in addition to another similar Kapton layer on the sample holder for double-containment, and a He-filled bag was placed between the sample holder and the detector. As a development from the protocol of Le Pape et al. (2020), we applied a continuous He flow inside the sample holder to prevent oxidation by air over the course of the experiment.

Substantial photo-reduction (beam-damage) was observed on the successive spectra obtained on soil samples during the experiment. To limit such effects, the HERFD-XANES spectra were acquired dynamically by continuous displacements over pristine areas of the sample pellet.

A qualitative analysis of the U M_4-edge HERFD-XANES spectra was done by comparing experimental spectra of the wetland soils with spectra of reference compounds. We selected autunite ($Ca(UO_2)_2(PO_4)_2 \cdot 10\text{-}12\ H_2O$) as U(VI) reference (Le Pape et al., 2020), triuranium octoxide U_3O_8 from the IMPMC chemical stocks containing in theory 67 % U(V) and 33 % U(VI) (Kvashnina et al., 2013) that was analyzed with the samples, and biogenic nanocrystalline uraninite UO_2 as U(IV) reference (Le Pape et al., 2020). This analysis is based on strong differences between the spectral features of U(VI)-uranyl compounds with three main fluorescence peaks at 3727.7, 3729.6 and 3733.4 eV due to the splitting of the *5f* orbitals, and the spectral features of U(V)- and U(IV)-uranate with single peaks at distinct energies (3727.5 and 3726.2 eV respectively) (see Figure 8b). The HERFD-XANES spectrum of U_3O_8 contains both U(V) and U(VI) contributions (two close peaks), and our biogenic UO_2 is partly oxidized (Le Pape et al., 2020), although composed of predominant U(IV) with a fraction of U(V) (Figure 8b).

2.5.4. Bulk Fe K-edge XANES and EXAFS analysis

The redox and speciation of iron (Fe) in four soil samples (2 of each core) was analyzed by XAS at the Fe *K*-edge on beamline 4-3 at the Stanford Synchrotron Radiation Lightsource (SSRL, SLAC National Accelerator Laboratory) in January 2020. Sample aliquots were mixed with cellulose and pressed as Kapton-covered pellets that were preserved from oxidation by air. The measurements were performed at liquid N_2 temperature in transmission detection mode. Incident energy was calibrated by setting the first inflection point of Fe metal foil at 7112 eV, using a double-transmission setup.

XANES and EXAFS spectra at the Fe *K*-edge were analyzed by LCF using the same code as for U L_3-edge data, using a set of model compound spectra chosen from a large database that includes several types of iron phosphate, carbonate, phyllosilicate, (oxyhydr)oxide, sulfide minerals in crystalline, nanocrystalline or amorphous state, as well as Fe(II) and Fe(III)-polyphosphate complexes and a natural Fe(III)-humate sample. After a PCA-TT analysis detailed in Supplementary Material, the best fits were obtained with a combination of a minimal set of 5 components that yielded good fits to the whole set of soil samples studied and accounted as reasonable proxies for the diversity of occurring Fe-bearing species: synthetic Fe(II)-triphosphate (Baumgartner et al., 2016) as a proxy of OM-bound Fe(II), natural Fe(III)-illite (Ildefonse et al., 1998; Merrot et al., 2019) and synthetic nano-Fe(II)-talc (Zeyen et al., 2019) as proxies for structural Fe(III) and Fe(II) in 2:1 clay minerals, synthetic Fe(III) 2-lines ferrihydrite (Maillot et al., 2011) and natural Fe(III)-humate (Cosmidis et al., 2014). As detailed in Supplementary Material, the use of the same five Fe components to fit our data both in XANES and in EXAFS ranges is expected to minimize the bias related to non-unique fit solutions. The LCF fit quality was estimated with a R-factor and a χ^2_R as described above for U L_3 data LCF.

3. RESULTS

3.1. Bulk mineralogical and chemical content of the soil cores

3.1.1. General geochemical and mineralogical description

Physicochemical parameters (pH, T, ORP, O_2, σ) were measured one year after core sampling at the exact location of the cores (Figure S4). At core C1 location, the stagnant water above the ground was slightly acidic (pH ~6.2) and showed dissolved O_2 and redox potential gradients decreasing down to 2.5 mg/L and 47 mV at the water-soil interface. At core C2 location, the water filling the core-hole was acidic (pH 5.5) and suboxic especially at depth (O_2 from 4 to 0.15 mg/L at 16.5 cm depth) but still with a positive redox potential (50-90 mV). It should be considered that O_2 could have been overestimated close to the water-air interface due to air diffusion during sampling (see *Supplementary Material* page 8). Hence, the bottom O_2 and ORP values in the sampling holes (Figure S4) may be more representative of the oxidation reduction potential at depth in these organic-rich soils, in which oxygen is likely consumed quickly by microorganisms in the pore waters. At both locations, the conductivity was low (~50 µS/cm).

C1 consists of three ~10 cm layers of dark brown (top) to beige (bottom) colors, overlying the granitic sand in the bottom 3 cm; C2 is homogenously dark brown in the upper part, the bottom granitic sand being met at 22 cm (Figure S1). Both cores mainly differ in their organic content as attested by TOC concentration profiles (Figure 2a). They display a similar mineral content composed of major granitic minerals, as shown by powder XRD patterns (Figure S5). C1 has a moderate and decreasing organic content from top to bottom (10-13 to 1.4 wt% TOC), concomitant with an increase in the proportion of detrital granitic material (represented by Al contents, Figure 2a). C2 is highly organic (~40 wt% TOC) in the upper section above the granitic sand met at 22 cm (Figure 2). C1 show a relatively constant C/N atomic ratio around 12.7, except at depth (26-28 cm) with a lower ratio of 9.5 (Figure S6), which may however be linked to higher uncertainties due to a low N content slightly above the limit of quantification. The C/N ratios are higher in core C2, increasing with depth from 17.2 to 25.6 (Figure S6).

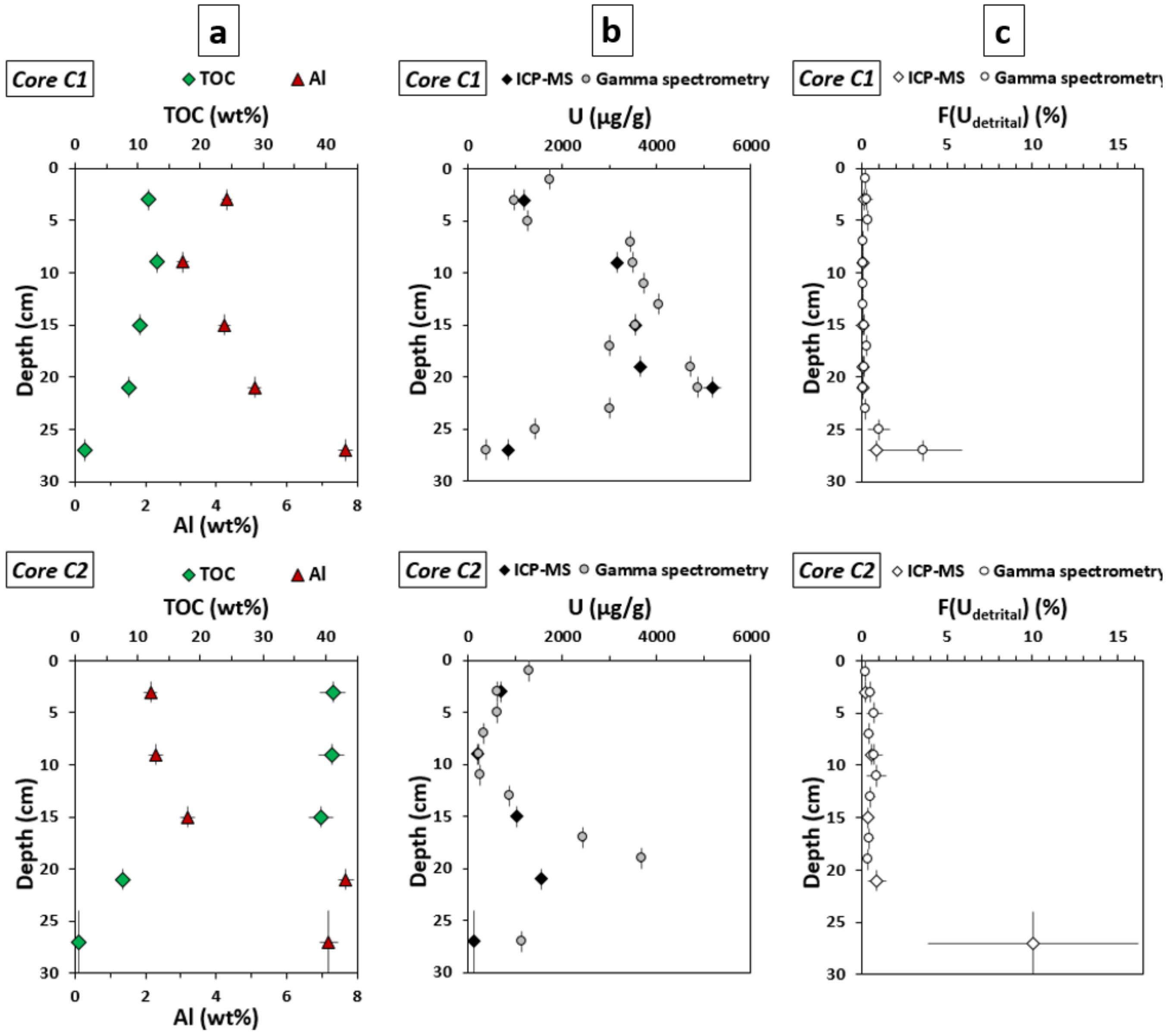

Figure 2 – Chemical composition of the wetland soils from cores C1 (top) and C2 (bottom). *(a) Total organic carbon (TOC, green diamonds) and Aluminum (Al, red triangles) contents; (b) Uranium content measured by ICP-MS after sample digestion (black diamonds) and by gamma spectrometry (gray circles); (c) Detrital U fraction ($F(U_{detrital})$) estimated from U/Th ratios measured by ICP-MS (diamonds) and gamma spectrometry (circles).*

3.1.2. Fe oxidation state and speciation

Depending on the Fe speciation, the Fe oxidation state in the soil cores may give indications on the soil redox conditions. The soils contain low Fe amounts, increasing with depth from 0.5 to 2.0 wt% in core C1 and from 0.3 to 1.5 wt% in C2. Results of the LCF analysis of the Fe *K*-edge XANES spectra, as reported in Table S1a, should be considered as more reliable than EXAFS ones for redox-state determination. They indicate moderate but detectable differences in the Fe oxidation state between the C1 and C2 cores (Table S1, Figure S7). In core C1, Fe is essentially present as Fe(III) (79 ± 8 % at 2-4 cm, 88 ± 3 % at 14-16 cm), while Fe is slightly more reduced in core C2 (31 ± 10 and 28 ± 8 % Fe(II) at 2-4 cm and 14-16 cm respectively).

A combined XANES and EXAFS LCF analysis (Figure S7a, Table S1a), guided by a PCA-TT analysis for EXAFS (Figure S7b, Table S1b), allowed us to propose an evaluation of Fe speciation using a minimal set of proxies for Fe-clays, Fe-oxyhydroxides and Fe-organic components. Although the contribution of these Fe species is subject to uncertainties (Table S1a), it appears that a significant proportion of Fe is hosted by clay minerals (represented by our Fe(III)-illite and Fe(II)-talc proxies) accounting for 30 to 85 ± 20% of total Fe in all samples. XANES LCF analysis also suggested a change in the nature of the additional Fe(II) and to a lesser extent Fe(III) species between the C1 and C2 core, with a better match to Fe-organic proxies in the C2 14-16 cm sample. These latter species could be consistently included as EXAFS fitting components, but with less statistical confidence than for XANES, as detailed in the note of Table S1a. Despite these analytical limitations, these results suggest that a significant fraction of Fe(II), and to a lesser extent Fe(III), could be ~~is~~ bound to organic matter in the C2 core, with 45 ± 30 to 68 ± 19 % of Fe accounted for by our Fe(II)-triphosphate and Fe(III)-humate proxies. Our interpretation of the XAS data is consistent with the significant differences in TOC contents of the two cores down to 20 cm depth (Figure 2a).

3.1.3. Uranium content

Major differences are observed in the uranium content of the two cores (Table 1, Figure 2). Core C1 displays very high U concentrations above 3000 µg/g between 6 and 24 cm – culminating at 20-22 cm with 5180 µg/g, with lower U at the top and bottom. C2 shows a distinct trend with U decreasing from 1280 to 200 µg/g in the upper 12 cm before reaching a peak U content of 3670 µg/g at 18-20 cm, at the transition between the organic-rich, fine-grained upper section and the organic-poor, coarse-grained bottom section, where U contents decrease down to 110 µg/g in the fine (sieved) fraction of the bottom granitic sand. The ICP-MS and gamma spectrometry measurements are overall in good agreement (Figure 2b); the little discrepancies are attributed to horizontal heterogeneity of the sample slices that were cut into two halves for distinct analyses (see Methods section 2.1.1).

As calculated from U/Th ratios, a negligible U fraction (< 1 %) is incorporated into detrital minerals, except in the granitic sand at the bottom of both cores, where up to 10 % of U in the fine-grained (sieved) fraction is detrital (Table 1, Figure 2c). This indicates that most U (> 99 % in general) is authigenic, i.e., was in the dissolved/colloid-sorbed form prior to its transport and accumulation in the wetland soils.

3.2. Radioactive disequilibria in the ^{238}U decay chain

Both cores show substantial disequilibria in the ^{238}U decay chain, highlighting differences in the mobility of U and its daughter radionuclides (Figure 3a). Gamma spectrometry measurements allowed the detection of ^{230}Th and ^{226}Ra isotopes that are strongly depleted with respect to their parent radionuclide ^{238}U (at the top of the radioactive decay chain), with (^{230}Th/^{238}U) and (^{226}Ra/^{238}U) activity ratios well below 1 (mostly below 0.3). An apparent regrowth over time is observed as both ratios increase with depth, with the exception of (^{226}Ra/^{238}U) in core C2 that stabilizes around 0.1 below 10 cm depth. Considering the high amount of authigenic U combined with low detrital U and total Th contents, we assume that most ^{230}Th measured in the wetland soils originates from onsite regrowth from ^{238}U. In other words, the fraction of ^{230}Th originating from upstream U decay followed by particle transport is considered negligible. This hypothesis is reinforced by high (^{230}Th/^{232}Th) ratios in the soil samples (see *Supplementary Dataset*), well above the detrital ratio of 0.83 (corresponding to a ^{238}U/^{232}Th atomic ratio of 0.26). Following this reasoning, ^{226}Ra is also expected to originate mostly from regrowth in the wetland soils.

(^{234}U/^{238}U) activity ratios also show a radioactive disequilibrium but in the opposite direction: here, the daughter isotope (^{234}U) is enriched compared to its parent (^{238}U), with activity ratios constantly around 1.10-1.11 (Table 1, Figure 3b). Such values are above the secular equilibrium value of 1, that is measured in the background granite (Lefebvre et al., 2021a). This ^{234}U excess indicates that U mainly originates from chemical erosion of the bedrock resulting in preferential leaching of ^{234}U because of alpha recoil, which is consistent with the authigenic origin of U attested by U/Th ratios, as also observed in the sediments of Lake Nègre (Lefebvre et al., 2021a, b).

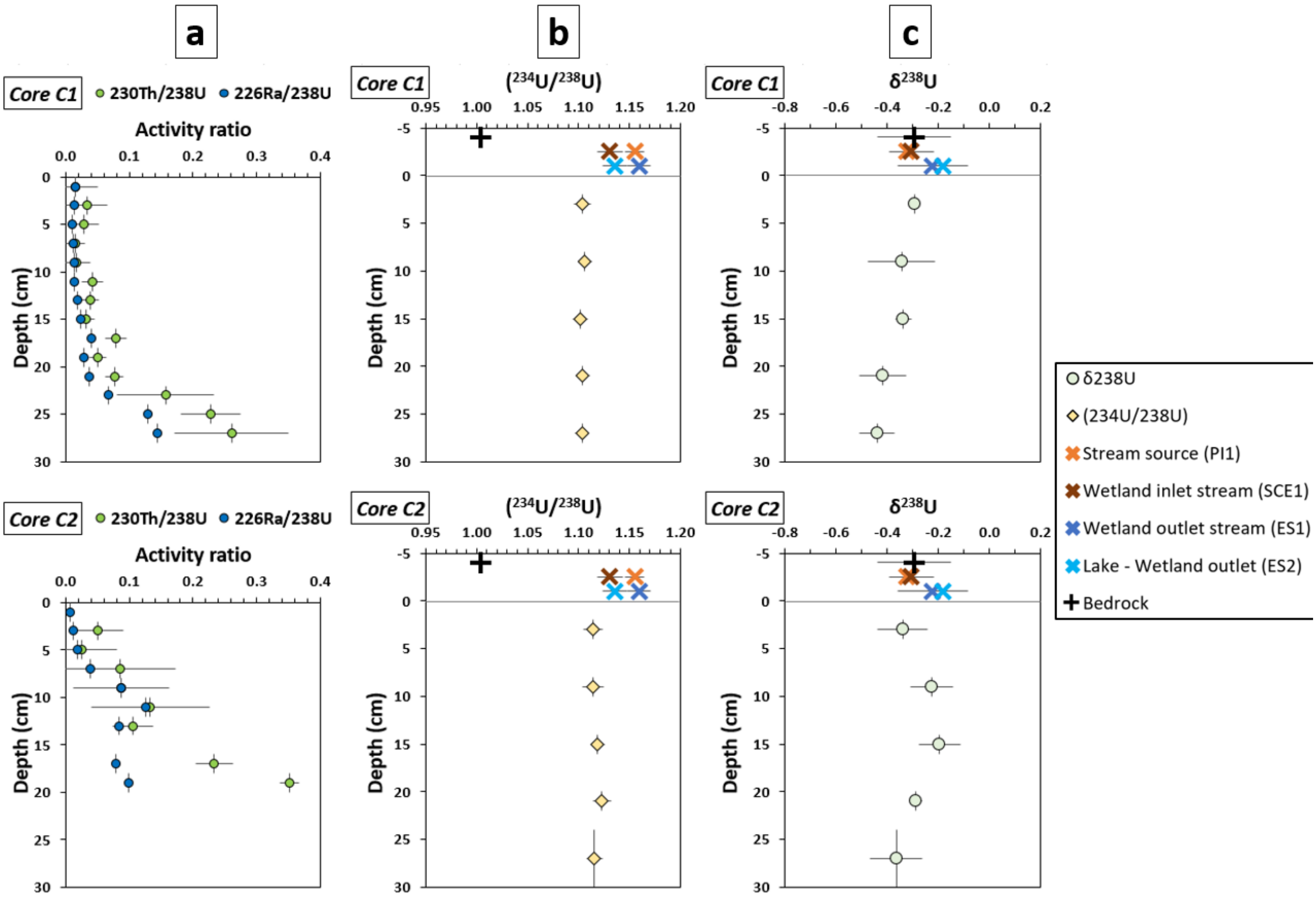

Figure 3 – Activity ratios and U isotopic ratios of the wetland soils from cores C1 (top) and C2 (bottom), compared to the bedrock and waters from the watershed. *(a) ($^{230}Th/^{238}U$) (green circles) and ($^{226}Ra/^{238}U$) (blue circles) activity ratios; (b) ($^{234}U/^{238}U$) activity ratios of the soils (orange diamonds) and (c) $\delta^{238}U$ isotopic signatures of the soils (light green diamonds), compared to isotopic signatures of the bedrock (black cross) and waters from the eastern stream up- and downstream of the wetland: at the spring (PI1, light orange cross), right upstream of the wetland (SCE1, dark orange cross), at the wetland outlet (ES1, dark blue cross) and 20 m downstream in the lake (ES2, light blue cross).*

Table 1 – Uranium concentrations, isotopic ratios, detrital fractions and oxidation states in bulk soil samples from cores C1 and C2. *Uncertainties are given as 2 or 3 standard deviations (σ). N.A.: not analyzed. R_f: R-factor indicating the U L_3-edge XANES fit quality. The U oxidation state of sample C2 24-30 cm (italicized) is uncertain due to low data quality. All XANES data in this table were acquired at DESY beamline P64, except data for samples C1 18-20 and 20-22 cm acquired at ESRF beamline BM23.*

Table 1 – Uranium concentrations, isotopic ratios, detrital fractions and oxidation states in bulk soil samples from cores C1 and C2. *Uncertainties are given as 2 or 3 standard deviations (σ). N.A.: not analyzed. R_f: R-factor indicating the U L_3-edge XANES fit quality. The U oxidation state of sample C2 24-30 cm (italicized) is uncertain due to low data quality. All XANES data in this table were acquired at DESY beamline P64, except data for samples C1 18-20 and 20-22 cm acquired at ESRF beamline BM23.*

Sample	U (µg/g)	2σ	δ^{238}U (‰)	2σ	(^{234}U/^{238}U)	2σ	F(U$_{detrital}$) (%)	2σ	% U(VI)	% U(IV)	3σ	Rf (.10^{-4})
C1 2-4 cm	1185	45	-0.29	0.01	1.104	0.008	0.16	0.10	58	42	3	0.6
C1 8-10 cm	3171	120	-0.34	0.13	1.106	0.007	0.09	0.05	81	19	3	0.6
C1 14-16 cm	3552	135	-0.34	0.03	1.102	0.007	0.10	0.06	65	35	4	0.9
C1 18-20 cm	3650	142	*N.A.*		*N.A.*		0.09	0.05	89	11	9	3.9
C1 20-22 cm	5184	197	-0.42	0.09	1.104	0.007	0.09	0.06	90	10	7	2.2
C1 26-28 cm	835	32	-0.44	0.07	1.104	0.007	0.87	0.54	90	10	7	2.5
C2 2-4 cm	678	26	-0.34	0.10	1.114	0.009	0.22	0.14	46	54	4	0.9
C2 8-10 cm	197	7	-0.22	0.08	1.114	0.011	0.59	0.36	78	22	13	9.0
C2 14-16 cm	1028	39	-0.20	0.08	1.119	0.007	0.39	0.24	80	20	5	1.3
C2 20-22 cm	1550	59	-0.29	0.03	1.123	0.009	0.90	0.55	61	39	3	0.6
C2 24-30 cm	113	4	-0.36	0.10	1.116	0.008	10.0	6.2	*73*	*27*	*39*	*77.0*

3.3. Uranium isotopic ratios δ^{238}U in soil cores

The uranium isotopic ratios $^{238}U/^{235}U$ – expressed as δ^{238}U – measured in the soils of cores C1 and C2 are homogeneous (Table 1, Figure 3c) and lie (within uncertainties) in the range of δ^{238}U values measured in the watershed bedrock (-0.29 ± 0.14 ‰, n=6) (Lefebvre et al., 2021a). In core C2, the isotope signatures seem to form a curved trend with higher δ^{238}U at mid-depth than in the upper and lower parts, but this trend is not statistically significant as uncertainties overlap. There is no clear relationship between δ^{238}U and U concentrations or ($^{234}U/^{238}U$) activity ratios (Figure S8).

3.4. Chemical and isotopic composition of the stream waters

3.4.1. Physicochemical parameters

As reported in the *Supplementary Dataset*, the water of the eastern stream (PI1, SCE1, ES1) show dissolved O_2 levels (from 7.9 to 6.7 mg/L) at or close to equilibrium with the atmosphere (~7.5 mg/L at 13-16 °C and 2350 m elevation). The conductivity is typical of mountainous streams with low values between 31.1 and 34.5 µS/cm. Redox potentials gradually increase from 157 to 216 mV along the stream course and are higher than that of the soil water at the location of cores C1 and C2. The pH of the stream is circumneutral (pH 6.9-7.4) and increases shortly after entering the lake at ES2, up to 8.2, which may be explained by photosynthetic activity in the lake surface water.

Lower O_2 (4.6-5.6 mg/L), σ and ORP as well as slightly acidic pH values (6.1 and 6.4) were measured in the western stream (E3 and ES3). At the time of sampling, this stream was resurging just before crossing the wetland and thus could not have fully equilibrated with the atmosphere.

3.4.2. Uranium partition in particulate, colloidal and dissolved fractions

In the ultra-filtered waters (SCE1, ES1, ES2), the partition of U among particles (> 0.2 µm), colloids (between 0.2 µm and 100 kDa) and "dissolved species" (< 100 kDa, including small colloids) was determined by measuring U concentrations (in µg/L) after the different filtration steps (Figure 4). For all other samples (PI1, E3, ES3, LAC-E1 and EXU1), a single 0.2 µm filtration step was applied and only the particulate U fraction was distinguished from the < 0.2 µm fraction, which includes colloidal and dissolved species. In the studied stream and lake waters, the particles and colloids are thought to be mainly organic (brown to green deposits on the filters), which could not be assessed by DOC measurements because of very low organic carbon contents (< 1 mg/L) barely above the instrumental detection limit.

Uranium concentrations in the creeks and in the lake are in the 2.3-13.2 µg/L range. These concentrations are well above the average U concentration in freshwater systems (~0.3 µg/L (Palmer and Edmond, 1993)) and are particularly elevated considering the absence of carbonate rocks (i.e., low dissolved inorganic carbon (DIC)) and the low dissolved Ca contents (~0.1 mM) of watershed waters. Such conditions should limit the formation of stable U calcium carbonato complexes (e.g., Maher et al., 2013). In all sampled waters, most of U (> 76 %) is transported in the colloidal and dissolved fractions (Figure 4). As the eastern stream flows down the mountain slope to the wetland and then to the lake (PI1 to SCE1 to ES1), U concentration decreases by ~24 % (12.6 to 9.6 µg/L) and the colloidal and particulate U fractions increase (from 0 to 24 % in particles). Twenty meters downstream from the stream outlet (ES2, in the lake), dilution in the lake causes a drastic drop of the U concentration (from 9.6 to 2.6 µg/L) and no more significant U-bearing particles are detected.

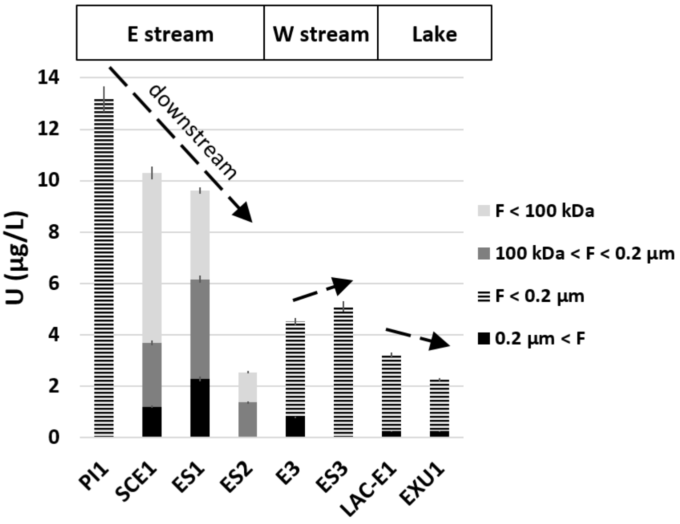

Figure 4 – Total uranium concentration in waters sampled up- and downstream of the wetland and its repartition among particulate (> 0.2 µm), colloidal (100 kDa < F < 0.2 µm) and dissolved fractions (< 100 kDa or < 0.2 µm, see Section 2.1.2). *PI1 is the spring of the eastern stream (E stream) feeding the wetland through SCE1, before flowing into the lake at ES1, diluted 20 m further at ES2. E3 is located upstream of the western stream (W stream) feeding the wetland, flowing into the lake at ES3. LAC-E1 was taken on the lake shore 100 m downstream from the wetland, EXU1 at the lake outlet. The sampling locations are illustrated in Figure 1.*

The western stream contains three times less U than the eastern one, and is slightly enriched in U (+ 13 %) after flowing across the wetland. The proportion of U borne by particles decreases from 18 to 1 % in the same interval. The lake water on the eastern shore (LAC-E1) and at the lake outlet has comparable U concentrations to ES2, however with significant particulate U fraction (8 and 11 % respectively).

3.4.3. Uranium isotopic composition of the water samples

The uranium isotopic composition (($^{234}U/^{238}U$) and $\delta^{238}U$) could be determined in the bulk (non-filtered) and 0.2 µm-filtered samples at SCE1, ES1 and ES2 (eastern stream), and in the bulk water of the eastern spring (PI1). As no significant difference was observed between the isotopic signatures of bulk and filtered samples, we further use the average values of both samples.

All waters display ($^{234}U/^{238}U$) activity ratios above that of soils from cores C1 and C2 (Figure 3b). The spring water (PI1) has a high ($^{234}U/^{238}U$) value of 1.155 ± 0.009, typical of U originating from weathered granite with ^{234}U supply by alpha recoil (e.g., Chabaux et al., 2003; Andersen et al., 2009). Further on the stream course upstream of the wetland (SCE1), the ($^{234}U/^{238}U$) ratio decreases to 1.131 ± 0.013. After flowing through the wetland (ES1), the stream ($^{234}U/^{238}U$) signature increases to 1.159 ± 0.011 and is finally lower again after dilution in the lake (ES2), at 1.136 ± 0.012.

The $\delta^{238}U$ signatures of waters shows lower variations: both waters sampled upstream of the wetland (PI1 and SCE1) have similar average $\delta^{238}U$ values of -0.32 ± 0.06 and -0.31 ± 0.09 ‰ respectively. After flowing through the wetland (ES1 and ES2), the stream displays a slightly higher $\delta^{238}U$ of -0.23 ± 0.13 and -0.18 ± 0.10 ‰ respectively; this difference is consistently observed among all measured $\delta^{238}U$ of the bulk and filtered samples (see *Supplementary Dataset*). All waters $\delta^{238}U$ signatures are indistinguishable from that of the soils within uncertainties, except for the lower half of core C1 where the soils are slightly isotopically lighter than the outlet waters ES1 and ES2 (Figure 3c).

3.5. Uranium distribution, redox and speciation in the soil samples

3.5.1. Identification of U-bearing phases by SEM, EPMA and micro-XRF mapping

High U content in the soils allowed the investigation of resin-embedded samples by SEM, revealing a variety of U-bearing phases detectable by EDXS. Representative examples of such U-rich particles are shown in backscattered electron imaging in Figure 5. Significant U amounts were detected by the means of the U M_α emission line, mainly in organic structures of various morphologies presenting a low intensity backscattering signal, such as vegetal remains (Figure 5a) or organic debris (Figure 5c,d) some with substantial U enrichment (Figure 5c,d), as well as organo-mineral aggregates (Figure 5b). Very rare occurrences of detrital grains containing traces of U and/or Th were found, such as zircon and monazite.

Additionally, thorough SEM-EDXS observation of the samples showed abundant diatom tests, especially in the C1 core, and scarce isolated sulfide grains (pyrite FeS_2 or $(Zn,Fe,Cu)S_x$) in core C1 at depth (18-20 cm) indicating the local occurrence of sulfidic conditions.

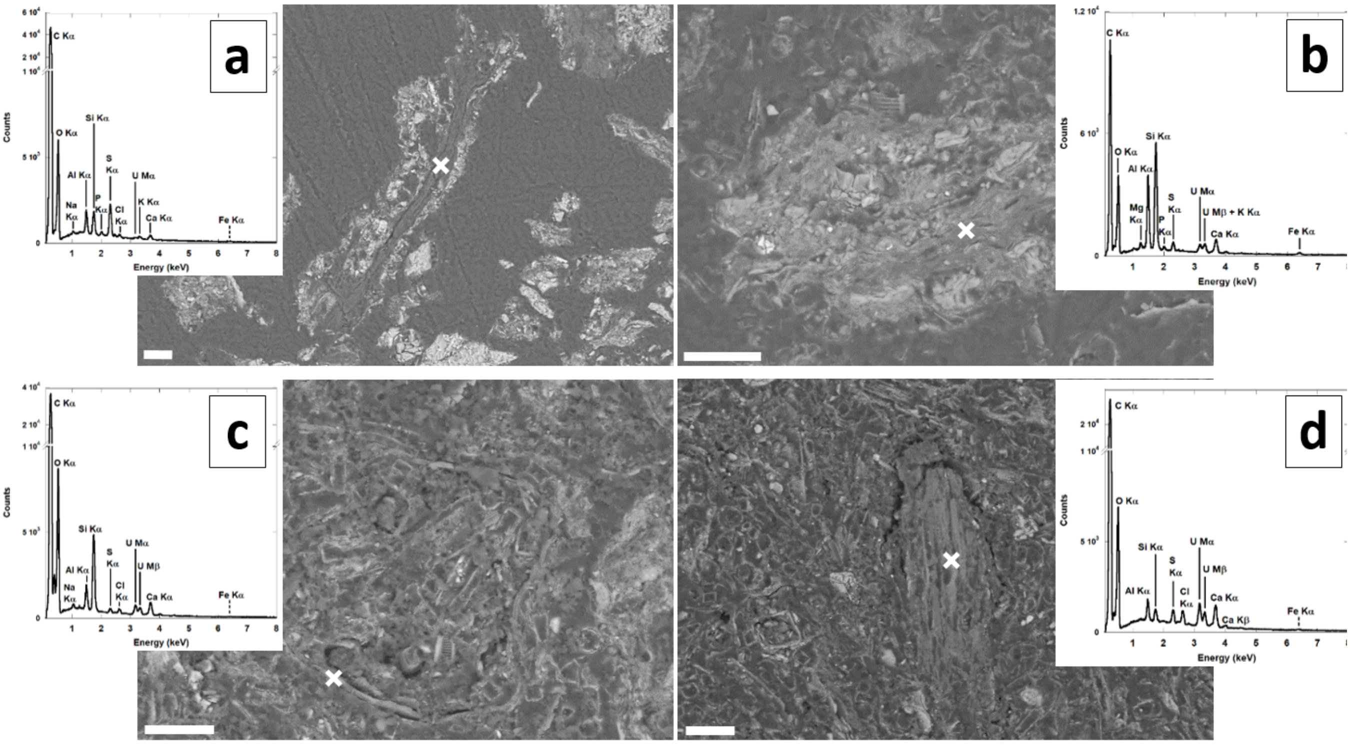

Figure 5 – SEM images and EDX spectra of uranium-bearing phases in the wetland samples. *(a) Vegetal remain containing trace U and coated by mineral grains, in sample C2 20-22 cm; (b) organo-mineral aggregate, which organic component contains U, in sample C1 20-22 cm; (c) U-rich organic debris in sample C1 14-16 cm; (d) U-rich organic debris in sample C1 18-20 cm. Diatom tests are abundant in core C1 (b-d). White crosses indicate EDX spectra spots. All scale bars are 20 µm.*

A few U-bearing phases were further analyzed by EPMA to quantitatively measure their chemical composition: two organo-mineral aggregates (100-200 µm wide) and a mineral-coated vegetal remain (200x500 µm) (Figure 6a and Figure S9). They show a heterogeneous U distribution, with U mainly associated to organic phases. U contents can reach as much as 3.25 at% in the vegetal remain displayed in Figure S9 with analyses reported in Figure 6d. Interestingly, we observe good correlations between the U, Ca and S contents (Figure 6c-e) in these organic soil constituents.

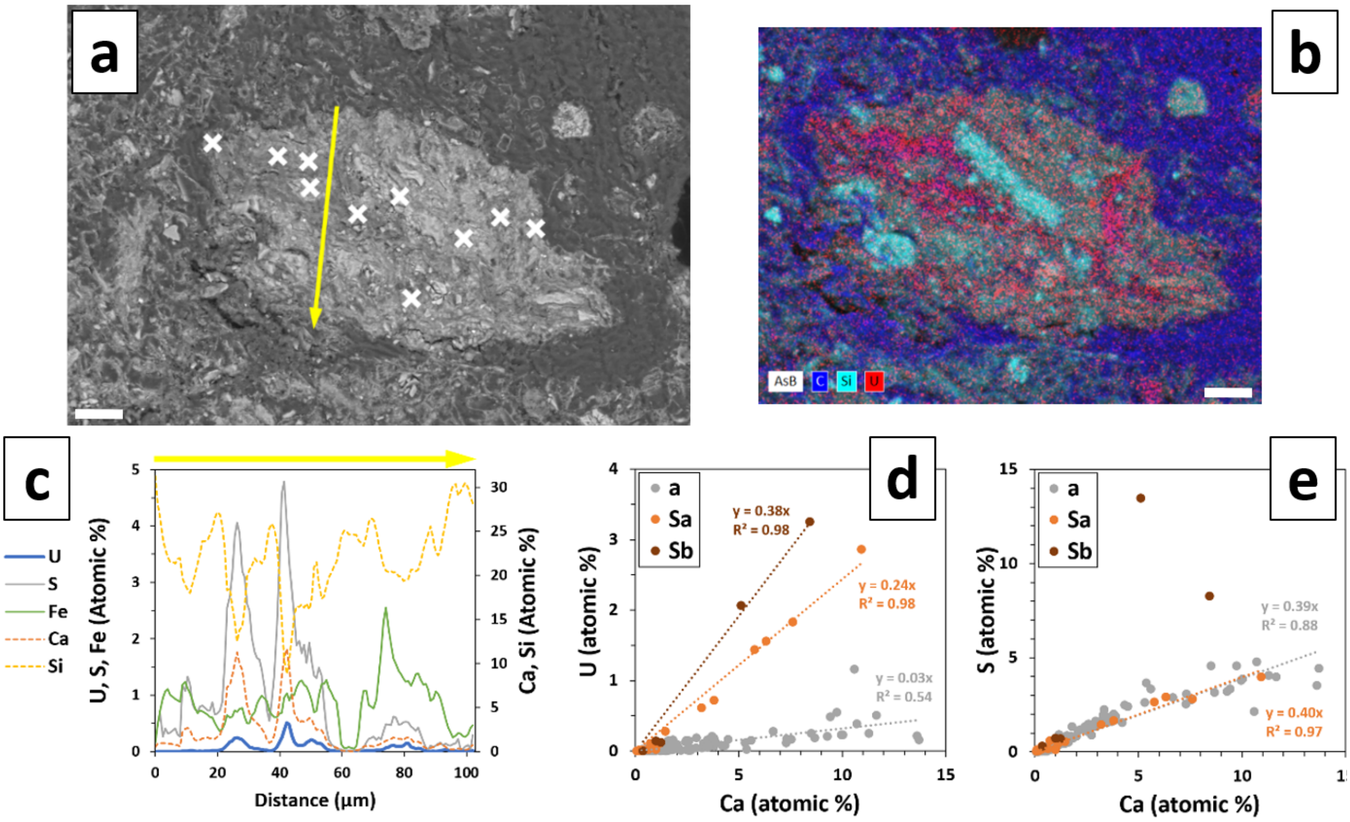

Figure 6 – Chemical micro-analyses by SEM-EDXS and EPMA of uranium-bearing phases in the wetland samples. *(a) Organo-mineral aggregate analyzed with EPMA (white crosses: spots, and yellow arrow: transect of 102-µm length, with 0.8 µm steps); (b) EDX mapping of C (blue), Si (turquoise) and U (red) in the same aggregate that is embedded in a C-rich resin. All scale bars are 20 µm. (c) Chemical composition (U, S, Fe – left axis, Ca, Si – right axis) along the yellow transect in (a). Covariations of U and Ca (d) and S and Ca (e) at all analyzed points on (a) including the transect, and on Figure S9a (Sa) and S9b (Sb); determination coefficients (R^2) and slopes of linear relationships are indicated.*

Further investigation of soil sample C1 18-20 cm (4726 µg/g U) was performed using synchrotron-based μ-XRF mapping in order to determine the micro-scale distribution of U with a better detection limit than SEM-EDX and EMPA, and to determine the redox sate of U in areas of interest (Figure 7). In the µ-XRF maps, uranium appeared to be broadly distributed within the soil matrix in which U could not be detected by SEM-EDXS. In Figure 7, it should be noted that the U-rich elongated pattern at the bottom of the upper map is likely a vegetal debris which fluorescence is enhanced by its thickness. Numerous thinner U-rich particles are spread over the sample matrix that contains low but detectable amounts of U.

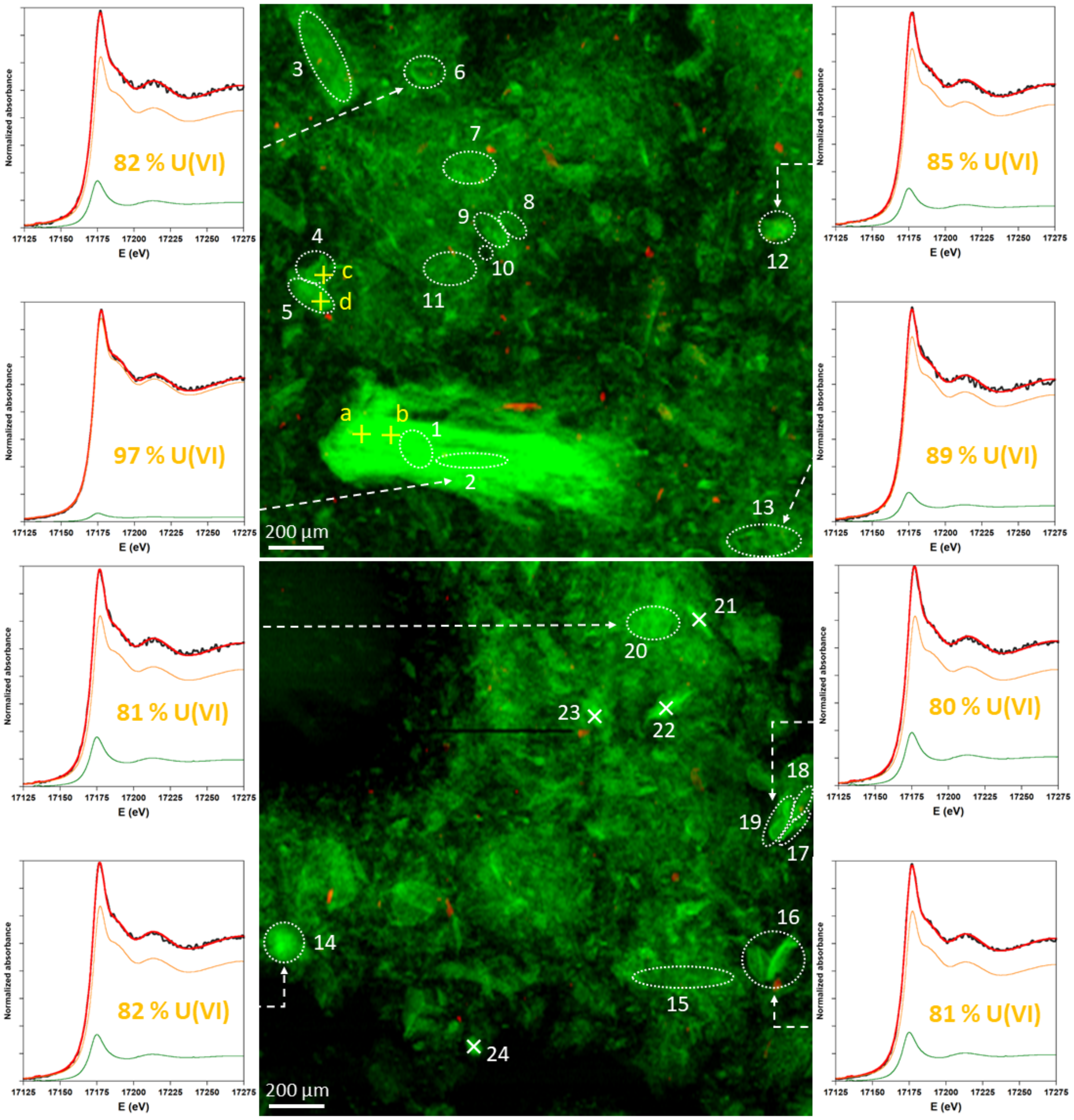

Figure 7 – Uranium-bearing phases observed by micro-XRF mapping and analyzed by micro-XANES*.* *These 2x2 mm µ-XRF maps show a diversity of U-bearing particles of various sizes and morphologies. U L_α and Fe K_α fluorescence lines intensities are displayed in green and red, respectively. Areas analyzed by µ-XANES at the U L_3-edge are delimited by white dashed lines and numbered from 1 to 20. Within each area, several scans collected on pristine spots were merged in order to limit beam-damage. In addition, four single spectra were acquired on U-rich spots and merged (21-24, white crosses). Examples of µ-XANES experimental spectra (black) and their corresponding LC-LS fit (red) with contributions of U(VI) (synthetic uranyl triscarbonato complex, orange) and U(IV) (reduced U-rich sediment NEG18-07 184-189 cm, green) components are shown on the sides for areas 2, 6, 12, 13, 14, 16, 19 and 20; the corresponding U(VI) proportions (% of total U) are indicated on each spectrum. U oxidation state obtained from LC-LS fits of the µ-XANES spectra (Figure S11) are reported in Table S3. Four spots lettered from a to d (yellow crosses, top) were chosen to estimate the beam-damage kinetics (Figures S2 and S3).*

3.5.2. Bulk and micro-scale U redox state determined by (μ-)XANES

The uranium oxidation state was determined by Linear Combination Fit analysis of U L_3-edge XANES spectra, after having chosen a single set of U(IV) and U(VI) model compounds that were relevant to nano-crystalline or non-crystalline U(IV) species encountered in soils and sediments and that were among the pure oxidized U(VI) and reduced U(IV) model compounds of our database (Table S2, Figure S10). According to these criteria, the best fits to the wetland soil XANES data were obtained using U(VI)-humic acid and U(IV)-sediment NEG18-07 189-194 cm as fitting components (Table S4, Figure S12).

Experimental U L_3-edge XANES spectra of bulk soil samples from cores C1 and C2 with their corresponding LC fits are displayed in Figure S12, with U(VI)-U(IV) proportions reported in Tables 1 and S4. The resulting U(VI) and U(IV) concentrations profiles are represented as a function of depth in Figure 8a. U(VI) is overall dominating at 58 to 90 % in most samples, with the notable exception of the C2 upper sample (2-4 cm), in which U(VI) and U(IV) are found in similar proportions. Overall, U(IV) proportions appear to be slightly higher in core C2 than in C1.

U M_4-edge HERFD-XANES spectra collected for five of the bulk soil samples corroborate the results of U L_3-edge XANES analysis. U(VI) appears to be dominant as indicated by absorption peaks at 3727.7, 3729.6 and 3733.4 eV similar to the U(VI)-autunite reference spectrum (Figure 8b). Some U(IV) is also present in all samples as attested by small shoulders at 3726.2 eV similar to the main absorption peak of uraninite. The lack of a shoulder at 3727.5 eV, main peak of U_3O_8, our U(V)-containing reference compound (Figure 8b), indicates that no detectable U(V) is present in our soil samples within the 10-15 % uncertainty range of the method.

Experimental U L_3-edge μ-XANES spectra of U-rich areas identified by μ-XRF in sample C1 18-20 cm are shown with their corresponding LC fits in Figures 7 and S11, with fitting results reported in Table S3. In accordance with the U redox state in the bulk sample (89 ± 9 % U(VI)), U(VI) dominates at all 21 analyzed areas (Figure 7), with proportions ranging from 80 to 97 %. Owing to the fit uncertainty (± 7-25 %; Table S3), U oxidation state in the 2x2 mm μ-XRF maps in Figure 7 can thus be considered homogeneous. Comparison of the XANES spectrum of the bulk sample (C1 18-20 cm) with the merge of all μ-XANES spectra yielded equal redox states within uncertainties, 86 ± 9 and 89 ± 9 % of U(VI) respectively (Figure S13).

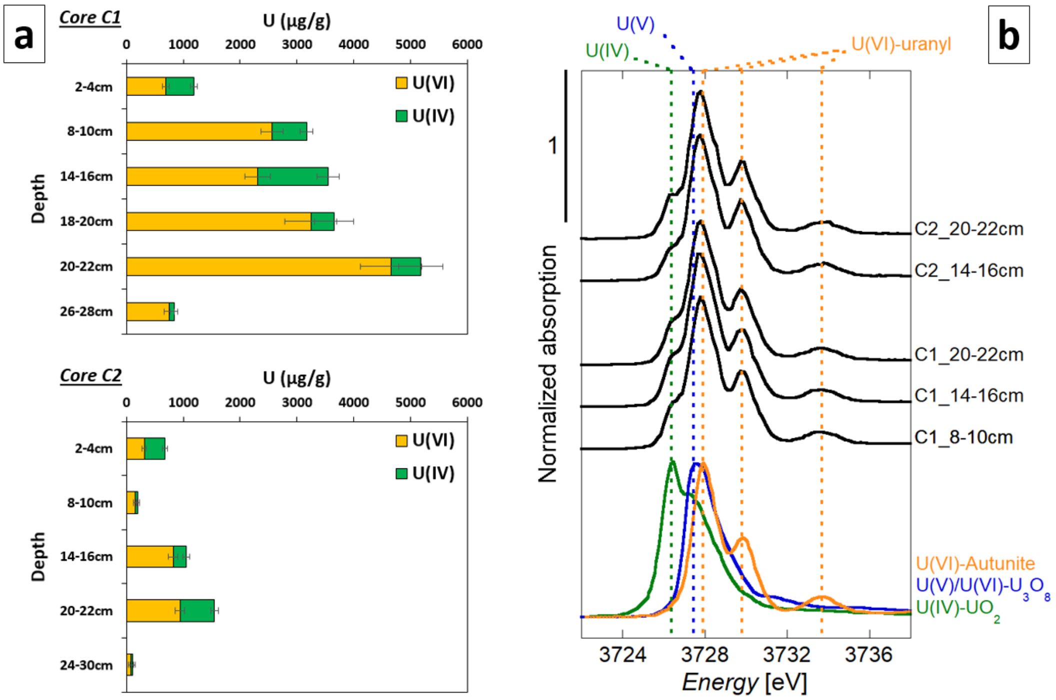

Figure 8 –Oxidation state of uranium in soil cores C1 and C2 determined by U L$_3$-edge XANES and U M$_4$-edge HERFD-XANES spectroscopies*. (a) Depth profiles along cores C1 and C2 of the U(VI) and U(IV) contents (in µg/g) determined from LC-LS fitting of U L$_3$-edge XANES spectra. U(VI) concentrations are shown in orange, U(IV) in green. Error bars represent 3σ uncertainties. Fitting results are reported in Table 1. (b) HERFD-XANES spectra at the U M$_4$-edge of reference compounds and soil samples from cores C1 and C2. Autunite was used as U(VI) reference, U_3O_8 contains 67 % U(V) and 33 % U(VI), and UO_2 was used as U(IV) reference (with a fraction of U(V)). Vertical dashed lines indicate the absorption features of U(IV) (green), U(V) (blue) and U(VI) (orange).*

3.5.3. Bulk U speciation determined by EXAFS

Following the Principal Component Analysis (PCA) of EXAFS spectra of our wetland samples, a minimum IND value (Malinowski, 1977) was obtained by including only the two first principal components that explained 98.4 % of the variance, thus suggesting that no more than 2 theoretical components should be necessary to explain our dataset. Samples C1 26-28 cm and C2 8-10 cm were not included in the PCA because their noisy EXAFS spectra led to overestimating the variance and would thus have introduced a bias in the PCA. Target Transform analysis was performed over our EXAFS spectra dataset of 20 model compounds. Results of this TT analysis are reported in Figure 9 and Table S5, in which a R-factor, $R_f = \sum [k^3\chi(k) - k^3\chi(k)_{\mathrm{TT}}]^2 / \sum [k^3\chi(k)]^2$, is used to compare the model compound spectrum to its target transform (Webb, 2005). The lowest R_f values were obtained for U noncrystalline species, such as U(IV) and U(VI) bound to organic or microbial compounds as well as clay mineral surfaces, indicating that these species were the most relevant to U speciation in our wetland samples. Based on these results, combinations of two or three of these model compounds spectra were tested for LCF analysis of the EXAFS spectra of the wetland soils samples.

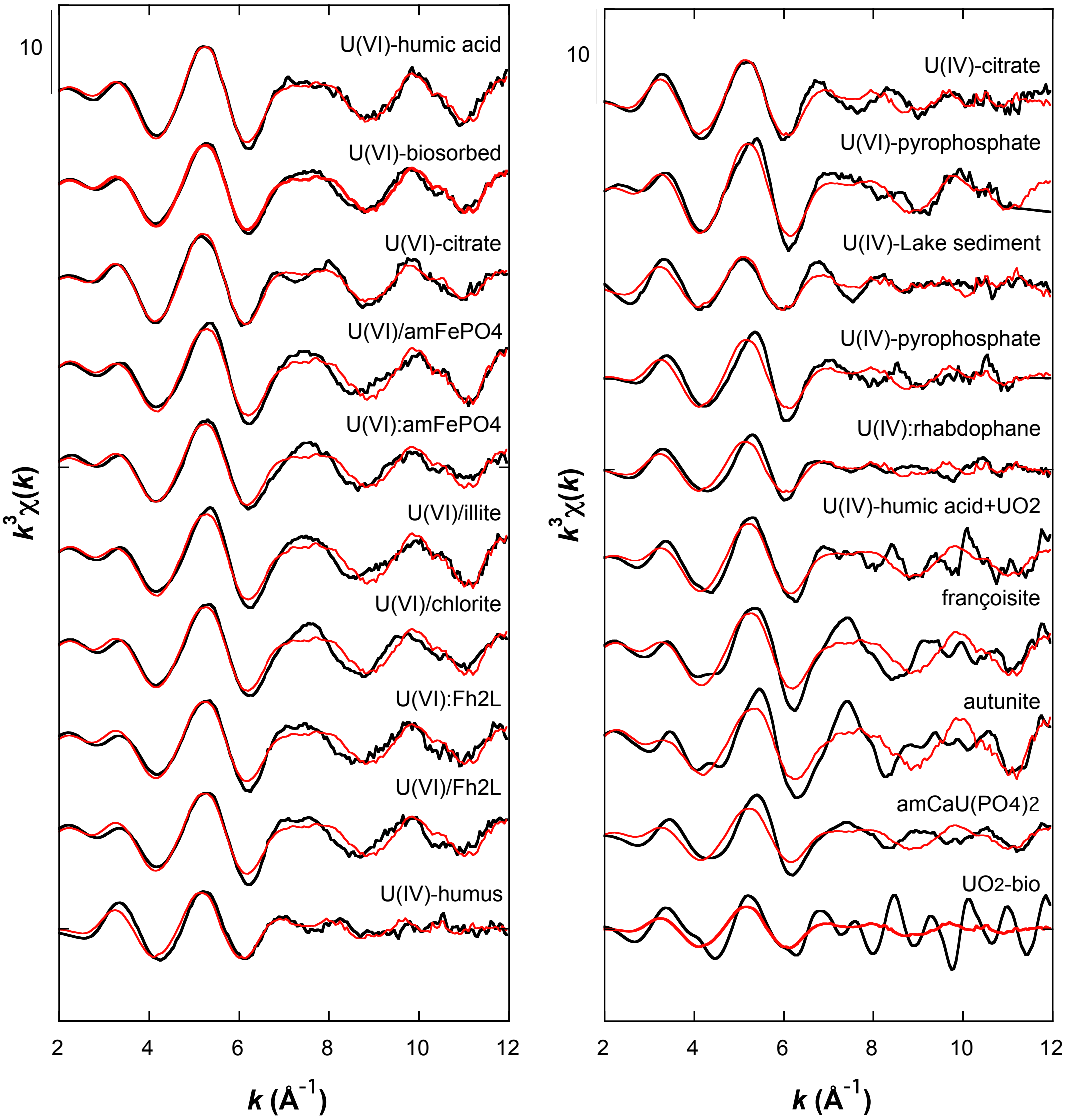

Figure 9 – Target Transform analysis of our set of model compounds U L_3-edge EXAFS spectra, using the two first components of the PCA analysis of our wetland soil samples data. *See Table S5 for quantitative results and for information and references on the reported model compounds spectra.*

The best LCF results were obtained by using two of the U(IV)-humus, U(VI)-biosorbed and U(VI)-citrate model compounds spectra as fitting components (Figures S14a and 14b; Table S6). Better matches to the wetland soil data could be obtained when including simultaneously the three components in the fit but with less reliable statistical results. Furthermore, fit combinations of two or three components including other model compounds, especially U(IV)-citrate, U(VI)-humic acid and U(VI)-sorbed to illite (Figure S10; Table S2), yielded satisfactory results for some samples (data not shown) but could not account for the whole set of wetland core samples studied and were thus not retained. Although being less accurate than XANES LCF for determining the U redox state (Table S4), EXAFS LCF results (Table S6) confirmed the overall higher proportion of U(IV) in the C2 core (Figure S14b) than in the C1 core (Figure S14a). Consistently with the PCA-TT analysis (Table S5, Figure 9), LCF analysis confirmed that the wetland soils EXAFS data could be reconstructed using solely non-crystalline U species as fitting components. The matching of the U(VI) component with either the U(VI)-citrate or U(VI)-biosorbed model compound spectra was mostly related to the shape of the spectrum in the 7-9 Å^{-1} *k*-range and likely relied on the number and distribution of equatorial U-O distances as suggested by the shell-by-shell fitting analysis presented thereafter (Table 2). The second neighbor contribution to the EXAFS was weak in all samples but showed a small peak centered at ~3 Å uncorrected for phase shift (Figures S14a and 14b), which we mainly attribute to C atom neighbors at ~3.3-3.5 Å, as discussed in the following shell-by-shell fitting analysis.

Shell-by-shell fitting of the unfiltered k^3-weighted EXAFS spectra was conducted over the 2-14 Å^{-1} *k*-range for the U-rich samples C1 18-20 cm and 20-22 cm, as well as for the model compounds that we used as fitting components for the LCF analysis (Table 2, Figure 10). For the U(IV)-humus model compound, data were only available to k = 12 Å^{-1}. The choice of second neighbors for the shell-by-shell fitting of soil samples data was first guided by the results of the shell-by-shell fitting of the U-organic model compound that were the most relevant to the system studied, according to PCA-TT-LCF analysis, as well as by μ-XRF, μ-XAS, SEM-EDXS and EPMA data reported above in the text. Shell-by-shell fitting of the k^3-weighted U L_3-edge EXAFS data was conducted in *k*-space and yielded also a good match in *R*-space as illustrated by comparing both the real part and magnitude of the FFT (Figure 10) and the Continuous Cauchy Wavelet Transform (Figure 11) of the experimental and calculated EXAFS spectra. Because it indicates in which *k*-region each FFT peak contributes to the EXAFS signal, CCWT analysis is particularly sensitive to the type of backscattering neighbor atom and thus helps deciphering between neighbors of U having close atomic numbers, such as C and P atoms (Morin et al., 2016; Stetten et al., 2018b). Beyond this qualitative information, the fit quality was checked using reduced chi-square calculations in both *k*- and *R*-space according to classical procedures reported in the Materials and Methods section. Alternative fit solutions were carefully evaluated and compared with those retained in Table 2 and Figure 10, according to statistical tests, as reported in Supplementary Material (Figures S15, S16 and S17).

For the two soil samples, shell-by-shell fitting results for the first neighbor O shells was consistent with the dominant U(VI) oxidation state of U in these samples. The coordination number (*CN*) value of the two axial O atoms was scaled to the proportion of U(VI) determined by

XANES analysis (Table 1), and kept fixed during the fitting procedure (Table 2), together with the associated multiple scattering paths. Two equatorial shells could be resolved with a total *CN* value of ~5-6 (Table 2). The second neighbor contributions to the EXAFS included a dominant contribution from C neighbors in monodentate (~3.5 Å) coordination, accompanied by P or Si neighbors in bidentate (~3.1 Å) coordination and U neighbors at ~4 Å (Table 2, Figure 10). Such U(VI)-P distance at 3.1 Å is in agreement with the results of quantum mechanical calculations reported by Kubicki et al. (2009) for aqueous bidentate uranyl-phosphate complexes, including organophosphate ones. Similar U-P bonding mode is also classically observed for U(IV) in humic substances (Stetten et al., 2018a), in products of microbial U(VI) reduction (e.g., Bernier-Latmani et al., 2010) and in U(IV)-phosphate crystal structures (Dusausoy et al., 1996; Rui et al., 2013; Morin et al., 2016; Stetten et al., 2018a). In our fits, this U-P path could be replaced by a U-Si path without changing the fit quality. Such a Si path at 3.1 Å has been for instance for proposed by Regenspurg et al. (2010) for U(VI) samples in their EXAFS study of U speciation in a pristine wetland. This U-P/Si path at ~3.1 Å could be also replaced by a U-C path at ~2.9 Å, with acceptable fitting results in *k*- and *R*-spaces, but this fit solution did not match the CCWT as well as the U-Si/P path at ~3.1 Å and could be discounted by an F-test at 95 % confidence (Figure S15). Attempts to include other elements such as Ca or Fe in second neighbor shells did not produce satisfying results. The detailed contributions to the EXAFS of the fitting shells retained in Table 2 and Figures 10 and 11 are exemplified in Figure S15, which displays the successive fitting results obtained when incrementing the number of fitting shells for the C1 20-22 cm sample, which results in a statistically significant fit improvement. To this regard, even more than the EXAFS and FFT curves, the CCWT analysis particularly shows that the U-C and U-P/Si second shells significantly contribute over the U-O_{axial} multiple scattering paths (MS). This analysis also clearly evidences the presence of a U-U path at ~4 Å in this sample. Hence, shell-by-shell fitting results for the C1 18-20 cm and 20-22 cm indicate that U is mainly present as mononuclear species bound to organic moieties in monodentate linkage geometry (U-C path at ~3.5 Å), as also proposed by Stetten et al. (2018a) in their study of a highly U-contaminated wetland. In addition, minor bidentate complexes with P (or Si) neighbors at 3.1 Å (or possibly C neighbors at 2.9 Å) are present. Eventually, we also observe the minor but detectable presence of condensed U phases as indicated by a U-U path at ~4 Å. This latter signal is particularly observed in the C1 sample at depth 20-22 cm, as attested by the fitting results (Table 2) and the CCWT analysis (Figures 11 and S15).

The shell-by-shell fitting results obtained for the U(VI)-biosorbed model compound were similar to those obtained for the two soils samples, albeit with a more pronounced contribution of C neighbors in monodentate (~3.5 Å) coordination and a similar contribution of U-P in bidentate (~3.1 Å) coordination (Table 2, Figures 10 and 11). This fit solution differs from that proposed by Seder-Colomina et al. (2015) and Stetten et al. (2018a) for the same model compound EXAFS spectrum from our database. These authors reported C neighbors at 2.9 Å and P neighbors at 3.6 Å, as a result of a fit in *k*-space and qualitative straightforward comparison in *R*-space, in agreement with the results reported in previous EXAFS studies of U(VI) sorption to bacterial cells (Merroun et al., 2005; Dunham-Cheatham et al., 2011). This latter set of C and P paths was actually complemented by a MS U-O-P path at 3.7 Å in the study of Seder-Colomina et al. (2015), following the fit solutions proposed by Kelly et al. (2002) and Llorens et al. (2012). A comparison of these different fit solutions is presented in Figure S16, including the CCWT of experimental and fit EXAFS curves. Comparing both FFTs and CCWTs suggests that the fit solution retained in Table 2 and Figures 10 and 11, with P and C shells at 3.1 and 3.5 Å respectively, is the most reliable, according to an F-test at 90% confidence (Figure S16), considering that only a limited number of shells can be included in the fit and even though the presence of additional C and P shells at 2.9 Å and 3.6 Å, respectively, cannot be excluded. Interestingly, quantum mechanical calculations conducted by Kubicki et al. (2009) on aqueous uranyl-phosphate complexes were reported by these authors to converge towards bidentate uranyl-phosphate bonding with a U-P distance at ~3.1 Å even when starting from a monodentate configuration. Moreover, in the same study, both monodentate U(VI)-C and bidentate U(VI)-P binding modes were found in significant proportions in calculated uranyl-organophosphate complexes. These findings further support our interpretation of the U L_3-EXAFS data of the soil samples and of the biosorbed model compound (Table 2, Figures 10, S15 and S16). In the present EXAFS analysis, beyond the inherent uncertainties in determining the exact distribution of U-C and U-P distances in such complex samples as U(VI) sorbed to bacterial cell walls, shell-by-shell analysis of EXAFS data show a similarity in the results obtained for the U(VI)-biosorbed model compound and for the C1 18-20 cm and 20-22 cm soil samples, which may explain the dominant contribution of this model compound in the LCF analysis of these soils samples (Figure S14a, Table S6).

The shell-by-shell fitting results obtained for the U(VI)-citrate model compound (synthesized in this study) indicated 6 equatorial atoms with a narrow distance distribution, and second neighbor C atoms showing a distribution of U-C distances in the 2.9-3.5 Å range (Table 2, Figure 10). According to Rossberg et al. (2009), the U-C path at ~2.9 Å is only significant with a *CN* > 1 since these authors detected this contribution in a C-free system. Consequently, the significance of this U-C path at 2.9 Å cannot be definitively proven from the EXAFS analysis of our U(VI)-citrate sample, even though such a distance corresponds to bidentate linkage of U to C moieties as in the structure of crystalline U(VI)-carboxylate compounds (Howatson et al., 1975; Denecke et al., 1998). This path was also proposed by Francis and Dodge (2008) for a U(VI)-citrate complex albeit misinterpreted by these authors as monodentate linkage, whereas this

2.9 Å path was considered negligible for U(VI)-acetate by Thompson et al. (1997), based on high-quality EXAFS data to *k* of 16 Å^{-1}. In contrast, the U-C distances at 3.3 Å and 3.5 Å with *CN* higher than 2 appear as the main second neighbor shells. These U-C distances in the 3.3-3.5 Å range can be attributed to monodentate linkage of U to C moieties, as it is common in the structure of crystalline U(VI)-carboxylate compounds (Howatson et al., 1975; Denecke et al., 1998) and as it has been predicted from first principles for U(VI)-carboxylate complexes (Schlosser et al., 2006). The presence of such C neighbors of U at 3.3 Å was also reported for a U(VI)-humic substance complex in the recent EXAFS study by Stetten et al. (2018a). The lack of observation of this monodentate U-C path at 3.3-3.5 Å in previous EXAFS studies of U(VI)-carboxylates and U(VI)-humic substances complexes may be related to the difficulty in distinguishing this second contribution from that of U-O$_{axial}$ MS paths in EXAFS data collected at room temperature (Denecke et al., 1997, 1998; Schmeide et al., 2003), as compared to EXAFS data collected at cryogenic temperatures in the study by Stetten et al. (2018a) and in this study (Figures 10, S15 to S17). In addition, the fit of our U(VI)-citrate compound was significantly improved when including a U-U path at ~4 Å for this high U loading sample (2 wt% U) (Table 2, Figure S17). This contribution is even more pronounced in the higher loading U(VI)-citrate sample by Francis and Dodge (2008), in which it was interpreted as a binuclear U(VI)-citrate complex.

Shell-by-shell fitting results for the U(IV)-humus model compound sample (Table 2, Figure 10) confirmed previous results reported by Stetten et al. (2018a) for the same sample, with again contributions from second neighbor P/Si atoms at 3.1 Å and C atoms at 3.5 Å, attributed to bidentate and monodentate binding to U(IV) in 8/9-fold coordination to oxygen.

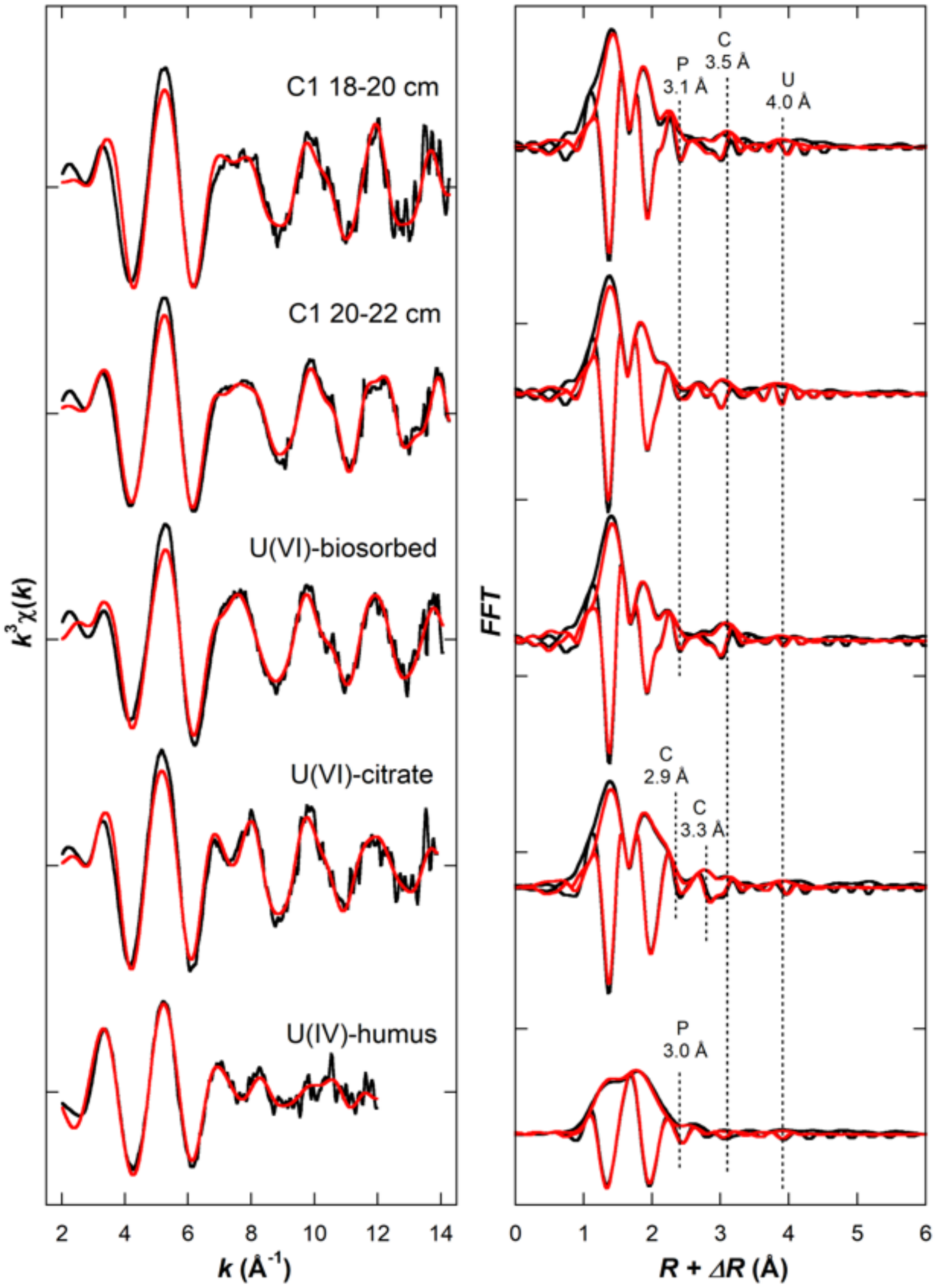

Figure 10 – Shell-by-shell fitting of unfiltered k^3-weighted U L$_3$-edge EXAFS data (left) and corresponding Fast Fourier Transforms (FFT, right) for wetland soil samples C1 18-20 cm and C1 20-22 cm and for the three model compounds used in our LCF analysis (U(VI)-biosorbed, U(VI)-citrate and U(IV)-humus). *The main second-neighbor contributions to the EXAFS are indexed by dotted vertical lines. The experimental and fit curves are displayed in black and red color respectively. The corresponding fitting parameters are reported in Table 2.*

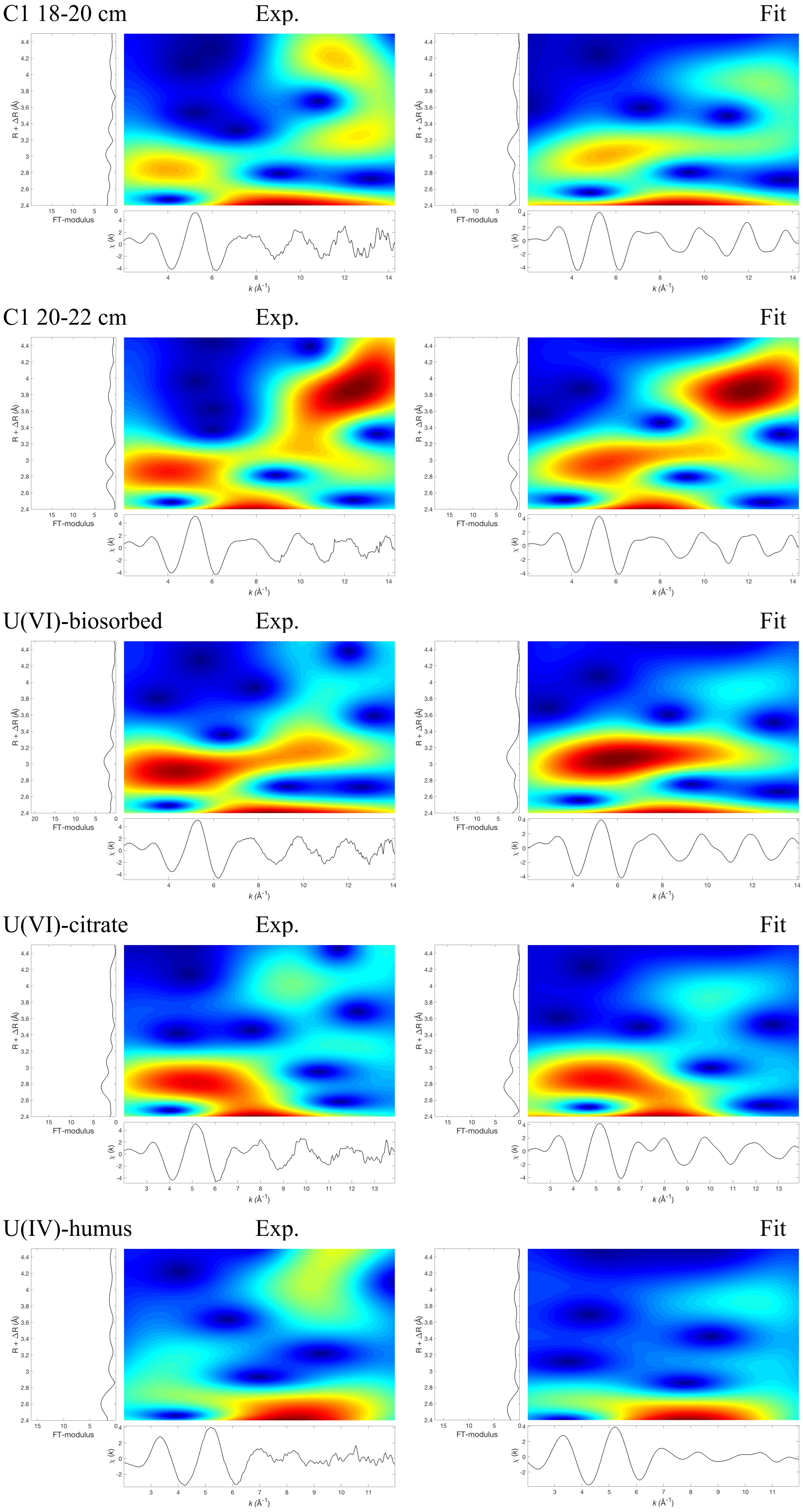

Figure 11 – Continuous Cauchy Wavelet Transform of experimental (exp, left) and shell-by-shell fitted (fit, right) unfiltered k^3-weighted U L_3-edge EXAFS data for wetland samples C1 18-20 cm and C1 20-22 cm and for the three model compounds used in our LCF analysis (U(VI)-biosorbed, U(VI)-citrate and U(IV)-humus). *The corresponding fits are plotted in Figure 10. Similar z-scales were used to allow comparison.*

Table 2 – Results of shell-by-shell fitting of U L_3-edge EXAFS data for wetland soil samples C1 18-20 cm and C1 20-22 cm, and selected model compounds (U(VI)-biosorbed, U(VI)-citrate and U(IV)-humus). *References for model compounds data are given in Table S5. The number of neighbors (CN) for the axial oxygen of uranyl ion together with associated multiple scattering paths (UO_{ax} MS including 2xUOO',2xUOUO' and 2xUOUO) were fixed to values expected from the U(VI)/U(IV) ratio determined from XANES LCF analysis (Table S4, Figure S12). The CN parameter values were fixed to acceptable values for second neighbor shells in order to provide physically meaning coordination geometry, in which the number of U-O bonds resulting from bidentate and monodentate complexes does not exceed the number of equatorial oxygen atoms. Fitting parameters included interatomic distance (R) of every backscattering path included, Debye-Waller parameter (σ) for each coordination shell, and overall energy difference (ΔE_0) between the user-defined and the ab-initio (Feff8) threshold energies. Parameter values indicated by (-) were linked to the parameter value placed above in the table and those followed by (*) were fixed. The fit quality was assessed by a reduced chi-square (Chi^2_R); uncertainties given in brackets relate to the last digit of each parameter and were estimated to 99.7 % confidence (3 sigma) (See Materials and Methods section). The U-U path is needed to match the CCWT (see Figure S15).*

Sample	path	*R* (Å)	*CN*	σ (Å)	ΔE_0 (eV)	Chi^2_R
C1 18-20 cm	U-O	1.797(4)	1.8*	0.051(2)	3.3(11)	17.2
	$U\text{-}O_{ax}$ MS	3.58*	5.4*	-	-	
	U-O	2.361(4)	2.9(3)	-	-	
	U-O	2.519(8)	2.5(4)	-	-	
	U-P/Si	3.06(2)	0.5*	0.054(11)	-	
	U-C	3.47(3)	2.0*	-	-	
	U-U	*4.06(2)*	*0.3**	*0.05(2)*	-	
C1 20-22 cm	U-O	1.775(3)	1.8*	0.055(2)	0.7(9)	7.5
	$U\text{-}O_{ax}$ MS	3.58*	5.4*	-	-	
	U-O	2.336(6)	2.7(2)	-	-	
	U-O	2.483(7)	2.3(3)	-	-	
	U-P/Si	3.07(1)	0.5*	0.058(7)	-	
	U-C	3.47(2)	2*	-	-	
	U-U	3.975(7)	0.3*	0.025(9)	-	
U(VI)-biosorbed	U-O	1.802(3)	2*	0.057(2)	4.3(11)	9.9
	$U\text{-}O_{ax}$ MS	3.58*	6*	-	-	
	U-O	2.350(7)	2.2(2)	-	-	
	U-O	2.506(9)	1.8(4)	-	-	
	U-P/Si	3.06(3)	0.5*	0.07(1)	-	
	U-C	3.50(2)	3*	-	-	
	U-U	*4.01(2)*	*0.3**	*0.06(2)*	-	
U(VI)-citrate	U-O	1.791(4)	1.8*	0.060(3)	1.9(12)	13.9
	$U\text{-}O_{ax}$ MS	3.58*	6*	-	-	
	U-O	2.373(7)	2.8(2)	-	-	
	U-O	2.506(8)	2.8(3)	-	-	
	U-C	2.95*	1*	0.06(2) -		
	U-C	3.32(3)	2.5*	-	-	
	U-C	3.48(2)	2.5*	-	-	
	U-U	*4.04(2)*	*0.5**	*0.07(2)*	-	
U(IV)-humus	U-O	1.73(2)	0.6*	0.06(1)	4.3(26)	13.3
	$U\text{-}O_{ax}$ MS	3.58*	1.8*	-	-	
	U-O	2.25(3)	4.1(9)	0.09(2)	-	
	U-O	2.41(3)	5.0(12)	0.06(1)	-	
	U-P	3.04(3)	0.5*	-	-	
	U-C	3.48(7)	1.0*	-	-	
	U-U	*3.93(5)*	*0.3**	*0.07(3)*	-	

The lower quality of the U L_3-edge EXAFS spectra of the other soil samples from cores C1 and C2 precluded a reliable shell-by-shell analysis. However, as indicated above, LC fitting of these EXAFS spectra produced similar results for all soil samples (Table S6, Figure S14) including the well-characterized C1 18-20 cm and 20-22 cm samples also analyzed by shell-by-shell fitting (Table 2, Figures 10, 11 and S15). Consequently, the molecular environment of U in all soil samples is expected to be dominated by contributions of bidentate and monodentate complexes with Si/P (~3.1 Å) and C (~3.5 Å) atom neighbors, respectively. The presence of minor U-U contributions is uncertain but cannot be excluded since these contributions were detected in the model compounds used for LCF (Table 2, Figures 10 and 11).

Altogether, the results of XAS analyses indicate that U(VI) and U(IV) are mainly sorbed to organic matter and potentially mineral surfaces (since Si neighbors could be present), in agreement with microscopic observations that show U association with organic soil constituents (Figures 5 to 7). The detection of U-U paths in some samples also suggests the minor presence of polymeric or condensed U phases.

3.6. Bicarbonate extraction of noncrystalline U

The 1 M bicarbonate extractions of soil samples resulted in the dissolution of most solid-state U: 92 to 96 % in samples from core C1 and 82 to 93 % in samples from core C2 (Figure 12). The bicarbonate-extracted U fraction is expected to be essentially composed of available noncrystalline U(VI) and U(IV) (Noël et al., 2019) but may also comprise some soluble crystalline U(VI) phases that may be extracted in the presence of high bicarbonate concentrations such as uranyl hydroxide (Bargar et al., 2008). The high percentages of extracted U are in accordance with the abundance of mononuclear U species detected by EXAFS spectroscopy. Moreover, extraction of 96% of U in sample C1 20-22 cm indicates that the condensed U phases detected by EXAFS (Figure 10) were almost completely extracted. This result suggests that these phases are either noncrystalline, consisting of polymeric/clustered U species dispersed and sorbed to the organo-mineral soil matrix, either crystalline but soluble in 1 M HCO_3^-.

Considering the uncertainty (± 9 % of total U) of the bicarbonate extraction method as estimated from replicates (see section 2.4), the residual – non extracted – fraction is almost negligible in core C1 (4-8 ± 9 % of total U), but more significant in core C2 (7-18 ± 9 % of total U). The residual fraction is expected to be composed of a minor fraction of detrital U (generally < 1 % of total U as estimated from U/Th ratios (Figure 2c)) and of sparingly soluble mineral or polymeric U-bearing phases. The detrital U fraction indeed accounts for only 1-11 % of the residual U in all samples, except for sample C2 24-30 cm where a large part of residual U (88 ± 61 %) is detrital.

LC fitting of the XANES spectra of two residual solids showed U oxidation states comparable to those of the initial samples (Table 1) within uncertainties, i.e. 81 ± 5 % U(VI) in the residue of C1 20-22 cm and 43 ± 9 % U(VI) in the residue of C2 2-4 cm (Table S7, Figure S18). This result shows that the residual U phases after bicarbonate extraction are not enriched in U(IV) with respect to the initial species. EXAFS spectra of the residual solids were of too low quality to allow proper shell-by-shell fitting of the data and to discuss the possible presence of crystalline U phases (*data not shown*).

Interestingly, 10 to 42 % of the initial ^{232}Th content was found to be leached by the 1 M bicarbonate solution. This indicates that in organic-rich wetland soils, a significant fraction of ^{232}Th may be associated to labile phases, for example to organic colloids (e.g., Bednar et al., 2004). As a consequence, the percentage of detrital U –estimated from ^{238}U/^{232}Th ratios to be mostly < 1 % (Table 1, Figure 2c) – may be slightly overestimated.

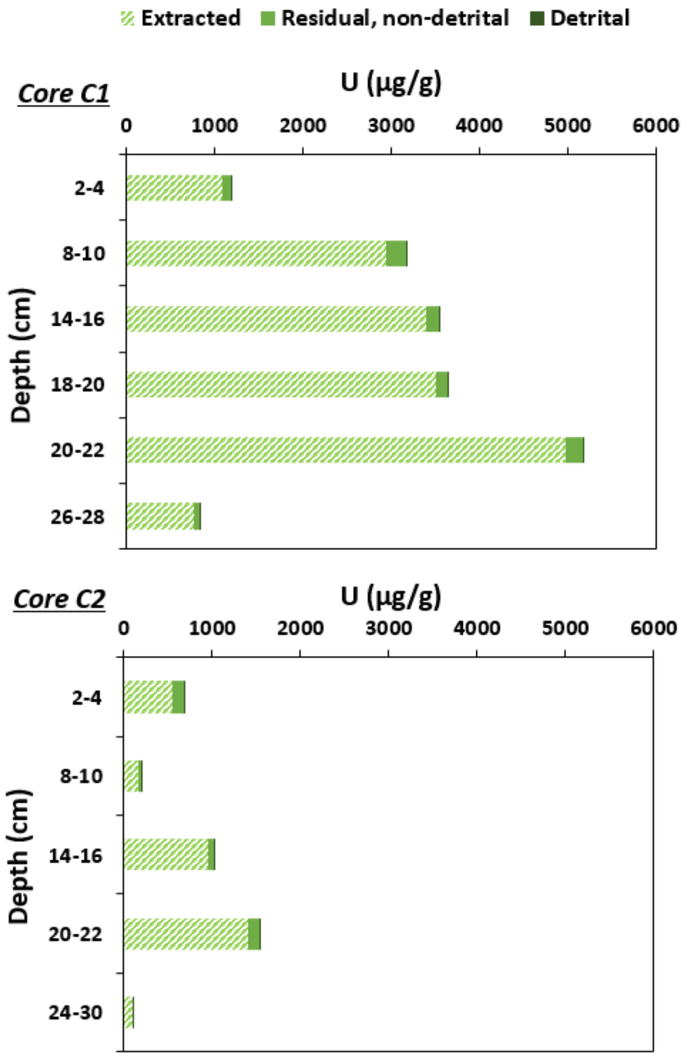

Figure 12 – Results of 1 M bicarbonate extractions of noncrystalline U in soil samples from cores C1 (top) and C2 (bottom)*. Repartition in µg/g U of the bicarbonate-extracted (light green), residual, non-detrital (medium green) and detrital (dark green) U fractions.*

4. DISCUSSION

The structure and chemistry of wetland environments such as that of Lake Nègre are largely driven by hydrological processes. First, at the wetland scale, the spatio-temporal dynamics of ground- and running surface waters exerts an important control on solutes and particles supply. Second, at the pore scale, complex reactive transport processes take place and regulate U mobility by controlling the spatio-temporal input of nutrients, oxidants and reductants, and by subsequently driving the local microbial activity. For instance, the local U supply may depend on the position relative to the spring input (e.g., Owen and Otton, 1995), and the lateral and vertical flow influence the soil redox dynamics and therefore the U mobility within the soil layers and outside of the wetland (e.g., Wang et al., 2013, 2014; Stetten et al., 2018a). For these reasons, and even in the absence of a detailed study of the wetland hydrology, the discussion below relies on some first order hypotheses on the wetland hydrology as a background rationale to interpret our dataset.

4.1. Biogeochemical characterization of the wetland soils

4.1.1. Environmental and redox conditions of the wetland soils

The studied wetland soils might actually be compared to alluvial sediments. They indeed developed on a flat area at the confluence of the two main creeks of the watershed that flow into Lake Nègre (Figure 1). In such a topographic setting, erosion is expected to be low and the main components of the wetland soils are thought to be (i) detrital materials (granitic primary and secondary minerals and vegetal debris) originating from upstream physical erosion and (ii) autochthonous materials, such as organic materials from plants and microorganisms that thrive in the wetland as well as secondary minerals formed by chemical weathering of the detrital granitic material. Such mineral phases have been identified in both cores by XRD and Fe *K*-edge XAS (Figures S5 and S7).

The texture of the cores points toward an intermediate soil-sediment status, with an apparent stratigraphy (also apparent in the radionuclide regrowth profile, Figure 3) that appears to be overlapped by soil water flow in the underlying granitic sand, and crossed by the vertical penetration of plant roots. Incidentally, the latter prevents any confident radiocarbon dating. For simplicity, we will continue to refer to “soils” in the following discussion.

The oxidation-reduction conditions in the soil pore water at both core locations are hardly predictable as our dissolved oxygen measurements may be overestimated close to the water-air interface. We hypothesize that the O_2 supplied by creeks or diffusing from the atmosphere is consumed by aerobic microbial activity in these organic soils. Overall, the soil redox conditions are probably controlled by seasonal variations of the water table, from fully reducing conditions when the soils are waterlogged (particularly during snowmelt) to more oxidizing conditions in dry periods (such as the time of sampling in September).

These global oxidizing conditions are in line with the Fe and U oxidation states observed in bulk soil samples, that are dominated by Fe(III) (69 to 88 % of total Fe, Table S1 and Figure S7) and U(VI) (Table 1, Figure 8). However, significant proportions of reduced, labile (organic-bound) Fe(II) and U(IV) species are noted, which is consistent with the fact that soil waters are overall suboxic (e.g., Maher et al., 2013).

4.1.2. Characterization of the soil organic matter

The two soil cores strongly differ in their organic matter content and composition. Core C1 contains relatively low OM amounts (~10 wt% TOC) with low C/N ratios around 12.7 (Figure S6), indicative of low-cellulose plants, probably driven toward lower C/N by abundant algae such as diatoms (Meyers and Teranes, 2001). The upper half of core C2 is much more organic-rich (~40 wt% TOC) because of abundant cellulose-rich plant remains characterized by high C/N (Meyers and Teranes, 2001). The measured C/N ratios in the wetland soils consistently match the range of "meadow-type environment" determined in our study of the Lake Nègre sedimentary OM (Lefebvre et al., 2021b). C/N values slightly higher than 20 – corresponding to "heathland/forest-type environments" – are recorded at depth in core C2. These ratios could indicate the past development of more cellulose-rich plants (such as shrubs) producing now-buried higher-C/N plant remains, potentially between 4.5 and 2.4 kyr before present (BP) (Lefebvre et al., 2021b).

These differences between cores C1 and C2 are attributed to their contrasting depositional environments (Figure S1). Core C1 was collected under stagnant water, where algae can thrive and where relatively few vegetal remains are produced and deposited. Core C2 was taken in the bed of a seasonal stream, where algae are scarcer and vegetal remains can settle along the flow path.

4.2. Uranium supply to the wetland

As the U concentrations measured in the wetland soils (up to 5200 µg/g) are far above the U content of the bedrock (2-6 µg/g, (Lefebvre et al., 2021a)), it is evident that U was transported from upstream in the watershed and then accumulated in the wetland soils. This is further supported by high U concentrations in the creeks (~10 µg/L). We hypothesize that U initially originates from an unidentified U-rich body with higher U content than the sampled granitic bedrock, either non-sampled or located beneath the surface, and releasing U through chemical erosion and transport in fracture networks of the granite (e.g., Schumann et al., 2017). Indeed, the high ($^{234}U/^{238}U$) activity ratios of creek waters and soils, above secular equilibrium

(Figure 3), unsurprisingly indicate that U originates from chemical erosion of the granitic bedrock and was-further transported as dissolved/colloidal species before binding to particles and accumulating in the wetland soils. This is corroborated by the very low detrital U content in the soil cores (Table 1, Figure 2), which supports the authigenic origin of U. As the stream waters are well oxygenated, U is presumably transported as U(VI) in running waters.

The apparent decrease in dissolved U concentrations along the eastern stream path (Figure 4) may be explained either by dilution from other creeks with lower U concentrations, or by U scavenging in the soils along the hydrological path (between PI1 and SCE1), including in the wetland itself (between SCE1 and ES1). The hydrological setting observed on the field at the time of sampling would support the second hypothesis, as no visible confluent creeks were found. Following this assumption, the upstream watershed soils and the wetland would most probably act as a partial U sink at the time of sampling. Along the eastern stream path, our measurements suggest that a fraction of uranium is scavenged in the soils while physical erosion leads to the transport of U-bearing particles (Figure 4). The drastic drop of U concentrations between sampling points ES1 (wetland outlet) and ES2 (20 m downstream in the lake) could be explained by dilution in the lake of the U-rich creek coupled to the deposition of large U-bearing particles on the lake platform (Figure 1). These observations are in line with our previous hypothesis stating that U was supplied to Lake Nègre sediments through soil erosion (Lefebvre et al., 2021b). One should however keep in mind that the analyzed waters only provide an instantaneous picture of the U budget at the time of sampling. A full understanding of the U cycle in the Lake Nègre watershed would require high frequency sampling throughout the entire seasonal hydrological cycle, including during high precipitation events, which was not achievable.

The U concentration in the western stream (points E3, ES3) appears to slightly increase after crossing the wetland (Figure 4). This observation could be explained by seeping of the stream water through the wetland soils leading to minor U export under dissolved species, as no significant U-bearing particles were detected at the outlet (ES3).

4.3. Modes of authigenic U accumulation

4.3.1. Sorption on organic matter likely governs U accumulation

The $\delta^{238}U$ isotopic composition of the soil samples from cores C1 and C2 was shown to be indistinguishable from the stream waters sampled up- and downstream of the wetland (Figure 3). If the sampled waters $\delta^{238}U$ were considered representative of the $\delta^{238}U$ of the U source to the wetland – which may be questionable but remains consistent regarding the similarity with the bedrock $\delta^{238}U$ –, the absence of any significant isotopic fractionation between aqueous and solid-phase U points toward U sorption to the soils as the dominant U scavenging mechanism. Uranium sorption to OM and soil minerals is indeed documented to result in a 0 to -0.4 ‰ isotopic fractionation, adsorbed U being lighter than aqueous U (Brennecka et al., 2011; Shiel et al., 2013; Dang et al., 2016; Jemison et al., 2016; Chen et al., 2020). Given the complexity of the soil matrix and considering potential U sorption on particles and colloids prior to scavenging in the wetland soils, it is not surprising to observe such low isotopic effects in the wetland. The measurement of slightly isotopically heavier U in the outlet waters compared to inlet water is in line with this sorption hypothesis. The presumed low formation of stable U(VI)-calcium carbonato complexes in the aqueous phase (because of low DIC and Ca in the creeks) may actually have favored U association with the solid phase. Conversely, higher carbonate concentrations (for example in case of a limestone bedrock) would likely have resulted in less U accumulation in the soils, although not provable here.

The identification of sorption as the dominant U scavenging mechanism would be consistent with the distribution, redox and speciation of U in the soils. Uranium was shown to be dispersed on a variety of phases, especially organic particles, with variable accumulations that are attributed to heterogeneous affinities of the adsorbing substrates for U (Figures 5 to 7). Most U is present as U(VI), indicating that U reduction may not be the only required mechanism for U partitioning in the solid phase. The U speciation determined by EXAFS to be dominantly mononuclear/noncrystalline, with U bound essentially to organic C moieties in monodentate coordination, and the high extent of U extraction by 1 M bicarbonate also support U sorption as the main U fixation process. Incidentally, U binding to C-rich molecules is thought to be the main cause of beam-damage, here U(VI) photo-reduction under the synchrotron beam, which we overcame by using cryogenic temperatures (Charlet et al., 2011) and/or moving on the sample between each measurement (see Materials and Methods section). Monodentate binding of U(VI) to C moieties of humic substances is consistent with the previous results of the EXAFS study of highly U-contaminated wetland soils (Stetten et al., 2018a, 2020) and differ from bidentate binding to C reported by Mikutta et al. (2016), which might be explained by a 10-fold lower U loading in this latter study. In this context, the observation of significant U-U paths by EXAFS could be interpreted as polymers or clusters of U atoms sorbed to organic moieties.

The high U contents recorded on organic particles including vegetal remains (Figures 5 to 7) – up to more than 3 at% – indicates the presence of binding sites with very high affinity for U. The type of U-binding organic moieties could not be determined, but we suspect that S and Ca play a major role, as all three elements contents are well correlated at the micro-scale (Figure 6).

4.3.2. Implications for U redox processes

One interesting finding of this study is that the U oxidation state at the micro-scale in one sample (C1 18-20 cm) was found to be homogeneous despite the variety of observed U-bearing phases (Table S3, Figure 7). This redox homogeneity could be interpreted as a direct consequence of the U speciation: the dispersion of sorbed U on OM surfaces (mononuclear or even polymeric, rather than incorporated into mineral grains) may favor a spatially homogeneous reduction rate by facilitating the electron transfers. It would thus enable all U atoms/complexes to follow the local redox conditions. To this regard, Stetten et al. (2020) have shown that U sorbed to OM in a heavily U-contaminated wetland could be fully reduced or oxidized within a few weeks during simulated flooding or drying periods, respectively.

Interestingly, the residual U fractions after 1 M bicarbonate extraction have a comparable U oxidation state to that of the initial soil sample and are still dominated by U(VI) (Tables 1 and S7, Figure S18). This residual fraction, which is non-detrital (see Section 3.6), may be composed of crystalline or highly polymeric U phases that could not be found by microscopic analyses but were detected by EXAFS, with significant U-U path contributions in most samples. These insoluble U phases contain high proportions of U(VI) and are therefore not reduced U(IV) crystalline phases such as UO_2 that could be expected as products of natural U(VI) reduction (e.g., Noël et al., 2017).

Although the U oxidation state is dominated by U(VI), significant proportions of U(IV) are detected. As U was supplied to the wetland by well-oxygenated streams, i.e., presumably in U(VI) forms, this means that a fraction of U(VI) was reduced to U(IV) within the wetland. A remaining question is the timing of such U(VI) reduction, before or after U(VI) sorption. $\delta^{238}U$ isotopic ratios are complementary of the redox and speciation analyses and may help in solving this issue. Direct reduction of aqueous U(VI) to U(IV) would likely have resulted in the incorporation of poorly soluble U(IV) in the solid phase following precipitation or sorption, and to an associated isotopic fractionation of ~1 ‰ (U(IV) being isotopically heavier than U(VI)), whether this reduction be abiotic or microbially-mediated (Basu et al., 2014, 2020; Stirling et al., 2015; Stylo et al., 2015; Dang et al., 2016; Brown et al., 2018). Conversely, the reduction of already adsorbed U(VI) should result in low fractionation factors ≤ 0.2 ‰ (Brown et al., 2018). Since we do not observe any isotope fractionation between stream waters and soils, neither between soils with different U(IV) contents, we infer that U(VI) reduction occurred after its sorption on the soil matrix. Sorption on organic matter may actually facilitate electron transfers, in conjunction with bacterial activity (Bargar et al., 2013; Bone et al., 2017b). The extent of U reduction may be driven by local redox conditions, either at the sample (centimetric) scale if the pore waters were actually anoxic, or in micro-environments where low permeability and high oxidant consumption rate favor reducing conditions. The detection of low but significant U(IV) in many U-bearing phases of sample C1 18-20 cm (Table S3, Figure 7) seems to favor the first hypothesis, but further μ-XANES investigation of other samples with higher U(IV) would be necessary to rule out or confirm the role of reducing micro-environments. Higher U(IV) proportions of ~50 % are notably measured in the upper (2-4 cm) samples of both cores C1 and C2. This observation could indicate that the soil redox conditions would be controlled by underground water flow. In particular, based on the stratigraphy of the cores and the mineral content of the observed layers, we could hypothesize that the more oxidizing conditions at depth could be linked to higher water circulation in more permeable layers, whereas lower permeability in the upper layers would result in lower oxidant penetration and thus more reducing conditions. Thus, subsurface water flow may also play a role in the vertical heterogeneity of U concentrations. In addition, higher microbial activity near the surface could also influence the soil redox conditions.

Anecdotally, the absence of significant U(V) contribution in the soil samples (Figure 8) as an intermediate state between U(VI) and U(IV) may be explained by the U speciation dominated by mononuclear OM-associated species. This speciation may have prevented any stabilization of the metastable U(V) which has been observed upon U incorporation or sorption in/to Fe minerals (Ilton et al., 2005, 2012; Pidchenko et al., 2017). This finding is in line with previous observations of no to very low U(V) in both U mining-impacted wetland soils (Le Pape et al., 2020) and pristine organic-rich soils (Fuller et al., 2020).

No major differences were noted in the processes of U accumulation in cores C1 and C2, despite a discrepancy in the amplitude of U accumulation (Table 1, Figure 2). We hypothetically attribute this difference to lower U supply at core C2 location than at core C1, possibly due to a different position with respect to the hydrological flow paths in the wetland network (Schumann et al., 2017). Core C1 was taken in a permanently flooded area where the water residence time is thought to be higher than at core C2, where a seasonal stream and underground water flow are the only potential U sources. Overall, our data indicate that the U accumulation mechanisms (U sorption to organic matter) are rather homogeneous at both cores locations despite their diverging mineralogical and organic compositions.

4.4. Uranium mobility in the wetland soils

4.4.1. Mechanisms of U mobility

The heterogeneous vertical distribution of U concentrations in cores C1 and C2 suggests that the underground water flow is involved in U accumulation. As a corollary, such water circulation may also induce horizontal and vertical U mobility in the wetland soils subject to hydrological fluctuations (Wang et al., 2014; Bone et al., 2017a; Stetten et al., 2018a; Lefebvre et al., 2019;

Noël et al., 2019). Seasonal changes in the soil water chemical composition and redox could indeed cause U desorption and further re-sorption elsewhere, i.e., downstream and/or in an upper or lower soil layer where conditions are favorable to U fixation.

Such mechanisms of U mobility in the wetland soils may provide a satisfactory explanation to the soil ($^{234}U/^{238}U$) ratios that are lower than the stream waters ratios (1.155 and 1.129) upstream from the wetland (Figure 3). The detrital U fraction at secular equilibrium being very low, such lower ratios could be explained by a loss of ^{234}U in the wetland soil, assuming that the measured ($^{234}U/^{238}U$) values in the upstream creeks are representative of the U source to the wetland soils. Even in noncrystalline U phases, the alpha-recoil effect during the production of ^{234}U from ^{238}U decay may make ^{234}U more mobile compared to its parent ^{238}U, especially through direct recoil of ^{234}Th into the pore water followed by its fast decay to ^{234}U, or by increasing the releasing ability of ^{234}U through damaging of the binding site (Chabaux et al., 2003). Following this hypothesis and assuming that the ($^{234}U/^{238}U$) ratio of U initially deposited in the wetland would be in the 1.13-1.15 range, the lower activity ratio (1.11) observed in the soils would roughly imply that a major fraction of ^{234}U produced by ^{238}U decay over the past ~10 kyr would have been leached. Such an assumption would be consistent with the estimated age of the oldest fraction of U found at depth in cores C1 and C2, as discussed in the next section. Alternatively, the low soil ($^{234}U/^{238}U$) ratios may possibly result from other sources of U to the wetland, for instance via subsurface water circulation.

4.4.2. Age constraints on U accumulation

The radioactive disequilibria in the ^{238}U decay chain (Figure 3a) were used to estimate age constraints on U accumulation, and roughly assess U and Ra losses caused by several thousand years of chemical erosion of the wetland. Although no precise geochronology can be established, the wetland is thought to have been developing since the end of the last deglaciation that occurred probably between 14,500 and 13,000 years BP in the Mediterranean Alps at this elevation (Brisset et al., 2015). The apparent regrowth with depth of radionuclides of the ^{238}U decay chain (^{230}Th, ^{226}Ra) (Figure 3a) can be partially interpreted based on this maximum age. The influence of radionuclide migration on ($^{226}Ra/^{238}U$) and ($^{230}Th/^{238}U$) activity ratios in the C1 and C2 cores was evaluated using a simple open system age model, detailed in the *Supplementary Material* (page 26) and based on the Bateman equations on which first-order rate constants (yr^{-1}) describing the release of radionuclides were added. We corrected the ($^{226}Ra/^{238}U$) and ($^{230}Th/^{238}U$) from their detrital components using ($^{238}U/^{232}Th$) ratios, assuming secular equilibrium in detrital minerals; the corrected ratios show little to no difference with raw ratios in most samples. Our qualitative model is based on the assumption that authigenic U (^{238}U and ^{234}U, with an activity ratio of 1.11) was deposited without any daughter ^{230}Th and ^{226}Ra

(see section 3.2). Then, the processes taken into account were losses of ^{226}Ra and ^{234,238}U and radioactive decay of the $^{238}\text{U} \rightarrow {}^{234}\text{U} \rightarrow {}^{230}\text{Th} \rightarrow {}^{226}\text{Ra}$ chain. ^{230}Th was considered as immobile. The intermediate daughter radionuclides of the decay chain (^{234}Th and ^{234}Pa) were ignored because their half-lives are too short to consider significant diffusion from the production site. Overall, our model relies on strong assumptions and thus only provides a qualitative overview of the age of U accumulation and of U and Ra mobility in the wetland soils.

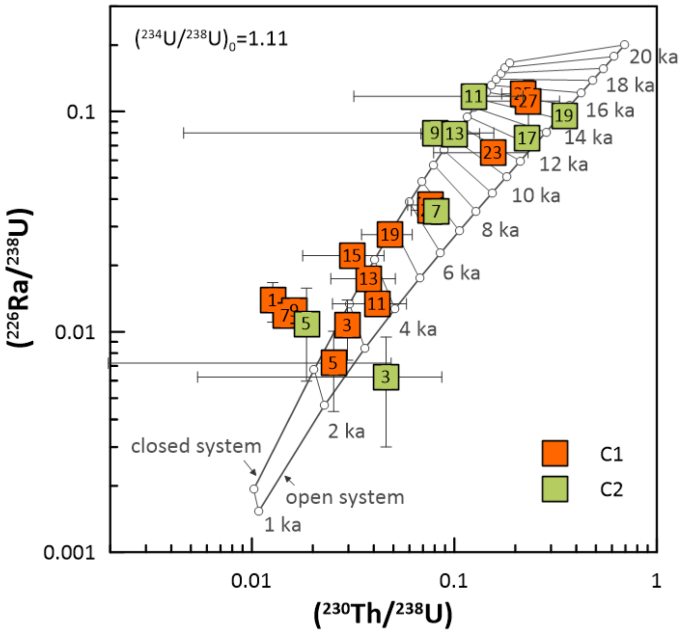

Figure 13 – Age constraints on U accumulation in soils of cores C1 (orange) and C2 (green) using radioactive disequilibria ((^{230}Th/^{238}U) and (^{226}Ra/^{238}U)). *Authigenic activity ratios (corrected from detrital components) are plotted with Concordia curves corresponding to a closed system (upper curve) and an open system accounting for U and Ra losses (lower curve), with corresponding ages (in ky). The numbers in squares correspond to sample depths in the cores (in cm). See text for details on the open system model.*

As shown in Figure 13, all authigenic (^{226}Ra/^{238}U) and (^{230}Th/^{238}U) activity ratios fall in the range of a closed system Concordia curve, confirming that ^{226}Ra and ^{230}Th likely originate from ^{238}U decay in the wetland soils after U accumulation. Even without accounting for U losses, the apparent maximum age of U deposition is consistent with the expected maximum age of the wetland at ~14500 y BP (Brisset et al., 2015). We then applied our open system model by allowing U and Ra loss constants to vary, in order to fit most of the data points within a maximum age of 14500 y (see *Supplementary Material* pages 26-27). In Figure 13, Ra loss results in a downward shift of the Concordia curve, while U release affect the age on a given point: the more U is lost, the younger the Concordia points.

Our model provides an estimation of the mean age of U accumulation in the wetland soils, which may be considered as an approximate age of soil formation, with high uncertainties due to radionuclide losses. Accordingly, the calculated soil ages span a range from 14.5 to 2-3 kyr BP and are consistent with the sample depths: deep soils generally appear to be older than upper soils (Figure 13). A few discrepancies are observed, that are attributed to differences in the soil texture and subsequent ability to accumulate and release U through hypothetic variations in groundwater circulation. For example, the soil in core C2 at 11 cm (sample 10-12 cm, containing 250 µg/g U) seems older than the underlying soil sample at 13 cm (12-14 cm, 860 µg/g U). This may indicate that the soil layer at 11 cm lost a significant U amount (and no significant Ra) and thus artificially appears older than the soil below.

A few upper soil samples, especially from core C1, appear to have gained Ra as they are plotted above the closed system Concordia (Figure 13). This suggests that while most soil layers released some U and Ra over the past thousand years – thus behaving as U and Ra sources –, some other layers acted as sinks and accumulated a fraction of the released radionuclides, highlighting their vertical mobility.

5. CONCLUSIONS

The present study combines a series of complementary geochemical and mineralogical techniques to provide a comprehensive view of the U scavenging mechanisms in two soil cores sampled in a natural mountainous wetland impacted by U supply for ~14500 y. In the Lake Nègre wetland, U likely originates from a (yet unidentified) U-rich source rock within the granite massif, the interaction of which with meteoric waters supplies dissolved U that is transported to the surface and subsequently to the wetland by running stream waters. This continuous U supply over thousands of years resulted in considerable U accumulation by organic complexation in the wetland soils, essentially in noncrystalline/mononuclear forms.

Bulk and μ-XAS revealed that U is mostly present as mononuclear U(VI) sorbed to carboxyl groups of organic matter, and, to a lesser extent, as polymeric U(VI) species at least in the U-richest samples (3000 – 5000 μg/g U). Both mononuclear and polymeric phases were extracted by 1 M bicarbonate (82-96 %). From a methodological standpoint, our extensive analyses using XAS at the U L_3- and M_4-edges shows that samples containing noncrystalline U species are affected by photo-reduction, which could be overcome by dynamic acquisition of short spectra on different spots. According to μ-XRF and MEB-EDX analyses, U was dispersed on a large variety of mostly organic structures, with different concentrations attributed to variable affinity of U for the binding sites. Measurement of U isotopic ratios (δ^{238}U) within the inlet/outlet waters and soils supported the idea that U sorption is the primary U scavenging mechanism in the studied organic wetland soil. Qualitative analyses of isotopic disequilibria in the U decay chain suggest that a fraction of U may have been scavenged for several thousand years in the wetland, especially in the deepest layers of the studied cores. Over such a long storage period, noncrystalline U species did not significantly evolve toward more crystalline phases. The minor detection of condensed, polymeric U species may be due to high U loadings in some of the studied soil layers rather than U aging. In contrast, an evolution toward U(IV)-Si polymeric species was recently reported as a result of diagenetic evolution of mononuclear U(IV) in the anoxic Lake Nègre sediments (Lefebvre et al., 2021a). The difference here is that the observed polymeric phases consist mostly of U(VI) and may have developed under oxidizing or fluctuating suboxic conditions.

The combination of mineralogical and isotopic techniques does not support significant direct reduction of aqueous U(VI) to solid U(IV) as the U scavenging process in the wetland soils. Such process, if any, is thus not responsible for the exceptional U accumulation in the Lake Nègre wetland, but rather is the sorption of U(VI) onto OM. The observed U(IV) proportions, that can reach ~50 % in the upper soil layers, are essentially due to reduction occurring after U(VI) sorption. The U oxidation state was found to be homogeneous at the micro-scale, which would suggest that the redox of mononuclear U is driven by the ambient redox conditions at the sample (centi- or millimeter) scale.

From the perspective of our deep investigations at the core scale, we suggest that the wetland soils act as an active reactor where chemically eroded U supplied by the watershed creeks is scavenged through sorption to organic matter and is then exported downstream to the lake through physical erosion. These organic soils are thus both sinks and sources of U, which in-and-out U transfers probably depend on seasonal climatic events that control erosion. At the time of the creeks water sampling, our observations suggest that the wetland was globally acting as a U sink. Better estimating the current U budget of the wetland would require to spatially monitor U transfers at the annual scale, including during extreme erosion events. Depending on the relative importance of erosion intensity and of the rate of U-binding sites renewal (vegetation and OM in general), the wetland could either be in steady state, i.e., scavenge as much U as it exports, either be a global sink of U (if vegetation develops more than is eroded) or a global source (if soil erosion is faster than renewal). As a consequence, the use of artificial wetlands to attenuate the environmental dissemination of U – although likely efficient in terms of global U budget – requires stewardship in the long term, especially during high precipitation events.

Acknowledgements

The authors thank Mathilde Zebracki, Pascale Blanchart, Didier Jézéquel, Fériel Skouri-Panet and Jean-Louis Reyss for their help in field sampling, Cyrielle Jardin, Lucas Nouveau, Gilles Alcalde, Emmanuelle Raimbault, Ludovic Delbès, Imène Estève, Barthélémy Julien and Michel Fialin for their help in laboratory analyses. This study was realized with the approval of the Director of the Parc National du Mercantour. We greatly acknowledge the Parc National and Marie-France Leccia for enabling access to and sampling in the Lake Nègre watershed. We are also indebted to the three anonymous reviewers and to Associate Editor Dr Annie Kersting for their fruitful comments on the manuscript.

We acknowledge the European Synchrotron Radiation Facility for provision of synchrotron radiation facilities and we would like to thank Thomas Buslaps and Joao Elias Figueiredo Soares Rodrigues for their assistance in using beamline BM23. Deutsches Elektronen-Synchrotron (Hamburg, Germany), a member of the Helmholtz Association of German Research Centers is acknowledged for the provision of experimental facilities and travel support. Parts of this research were carried out at PETRA III beamline P64 and we thank Wolfgang Caliebe for assistance during experiments. We acknowledge SOLEIL for provision of synchrotron radiation facilities on beamline MARS under proposal 20191337. We thank Ryan Davis, Matthew Root and Marcia Torres for their assistance in measurements and sample management at Stanford Synchrotron Radiation Lightsource (SSRL) beamline 4-3. The SSRL, Stanford Linear Accelerator Center National Accelerator Laboratory, is a national user facility supported by the United States Department of Energy, Office of Science, and Office of Basic Energy Sciences under Contract No. DE-AC02-76SF00515. We acknowledge the France–Stanford program "International Collaboration for Mitigating Mine Wastes for Improved Groundwater" for travel support.

This work was supported by IRSN through collaborative research program n° LS 20942, and by the Programme National EC2CO-BIOHEFECT/ECODYN (PUMA). Parts of this work were supported by IPGP multidisciplinary program PARI and by Paris–IdF Region SESAME Grant no. 12015908. This study contributes to the IdEx Université de Paris ANR-18-IDEX-0001. This is PATERSON, the IRSN's mass spectrometry platform, contribution no. 11.

Appendix A. Supplementary Material

Supplementary text, figures and tables: field sampling, additional chemical and mineralogical soil data, additional XAS data, U decay model.

XAS and μ-XRF data acquired at ESRF beamline BM23 will be available online from 2024 at DOI: 10.15151/ESRF-ES-439498784

REFERENCES

Abdelouas A. (2006) Uranium Mill Tailings: Geochemistry, Mineralogy, and Environmental Impact. *Elements* **2**, 335–341.

AERMC (2008) *Etude paléolimnologique sur 8 lacs du district Rhône-Méditerranée. Mise en place d'éléments de référence pour les lacs des 9 Couleurs, d'Anterne, de Chalain, de Lauvitel, Nègre, de Remoray, du Vallon et de Vens 1er, Années 2007-2008.*, Agence de l'eau Rhône, Méditerranée et Corse.

Alessi D. S., Uster B., Veeramani H., Suvorova E. I., Lezama-Pacheco J. S., Stubbs J. E., Bargar J. R. and Bernier-Latmani R. (2012) Quantitative Separation of Monomeric U(IV) from UO2 in Products of U(VI) Reduction. *Environ. Sci. Technol.* **46**, 6150–6157.

Andersen M. B., Erel Y. and Bourdon B. (2009) Experimental evidence for 234U–238U fractionation during granite weathering with implications for 234U/238U in natural waters. *Geochim. Cosmochim. Acta* **73**, 4124–4141.

Andersen M. B., Stirling C. H. and Weyer S. (2017) Uranium Isotope Fractionation. *Rev. Mineral. Geochem.* **82**, 799–850.

Ankudinov A. L., Ravel B., Rehr J. J. and Conradson S. D. (1998) Real-space multiple-scattering calculation and interpretation of X-ray-absorption near-edge structure. *Phys. Rev. B* **58**, 7565–7576.

Bargar J. R., Bernier-Latmani R., Giammar D. E. and Tebo B. M. (2008) Biogenic Uraninite Nanoparticles and Their Importance for Uranium Remediation. *Elements* **4**, 407–412.

Bargar J. R., Williams K. H., Campbell K. M., Long P. E., Stubbs J. E., Suvorova E. I., Lezama-Pacheco J. S., Alessi D. S., Stylo M., Webb S. M., Davis J. A., Giammar D. E., Blue L. Y. and Bernier-Latmani R. (2013) Uranium redox transition pathways in acetate-amended sediments. *Proc. Natl. Acad. Sci.* **110**, 4506–4511.

Basu A., Sanford R. A., Johnson T. M., Lundstrom C. C. and Löffler F. E. (2014) Uranium isotopic fractionation factors during U(VI) reduction by bacterial isolates. *Geochim. Cosmochim. Acta* **136**, 100–113.

Basu A., Wanner C., Johnson T. M., Lundstrom C. C., Sanford R. A., Sonnenthal E. L., Boyanov M. I. and Kemner K. M. (2020) Microbial U Isotope Fractionation Depends on the U(VI) Reduction Rate. *Environ. Sci. Technol.* **54**, 2295–2303.

Baumgartner J., Menguy N., Gonzalez T. P., Morin G., Widdrat M. and Faivre D. (2016) Elongated magnetite nanoparticle formation from a solid ferrous precursor in a magnetotactic bacterium. *J. R. Soc. Interface* **13**, 20160665.

Bednar A. J., Gent D. B., Gilmore J. R., Sturgis T. C. and Larson S. L. (2004) Mechanisms of Thorium Migration in a Semiarid Soil. *J. Environ. Qual.* **33**, 2070–2077.

Bernier-Latmani R., Veeramani H., Vecchia E. D., Junier P., Lezama-Pacheco J. S., Suvorova E. I., Sharp J. O., Wigginton N. S. and Bargar J. R. (2010) Non-uraninite Products of Microbial U(VI) Reduction. *Environ. Sci. Technol.* **44**, 9456–9462.

Bone S. E., Cahill M. R., Jones M. E., Fendorf S., Davis J., Williams K. H. and Bargar J. R. (2017a) Oxidative Uranium Release from Anoxic Sediments under Diffusion-Limited Conditions. *Environ. Sci. Technol.* **51**, 11039–11047.

Bone S. E., Cliff J., Weaver K., Takacs C. J., Roycroft S., Fendorf S. and Bargar J. R. (2020) Complexation by Organic Matter Controls Uranium Mobility in Anoxic Sediments. *Environ. Sci. Technol.* **54**, 1493–1502.

Bone S. E., Dynes J. J., Cliff J. and Bargar J. R. (2017b) Uranium(IV) adsorption by natural organic matter in anoxic sediments. *Proc. Natl. Acad. Sci.* **114**, 711–716.

Brennecka G. A., Wasylenki L. E., Bargar J. R., Weyer S. and Anbar A. D. (2011) Uranium Isotope Fractionation during Adsorption to Mn-Oxyhydroxides. *Environ. Sci. Technol.* **45**, 1370–1375.

Brisset E., Guiter F., Miramont C., Revel M., Anthony E. J., Delhon C., Arnaud F., Malet E. and de Beaulieu J.-L. (2015) Lateglacial/Holocene environmental changes in the Mediterranean Alps inferred from lacustrine sediments. *Quat. Sci. Rev.* **110**, 49–71.

Brown S. T., Basu A., Ding X., Christensen J. N. and DePaolo D. J. (2018) Uranium isotope fractionation by abiotic reductive precipitation. *Proc. Natl. Acad. Sci.* **115**, 8688–8693.

Campbell K. M., Kukkadapu R. K., Qafoku N. P., Peacock A. D., Lesher E., Williams K. H., Bargar J. R., Wilkins M. J., Figueroa L., Ranville J., Davis J. A. and Long P. E. (2012) Geochemical, mineralogical and microbiological characteristics of sediment from a naturally reduced zone in a uranium-contaminated aquifer. *Appl. Geochem.* **27**, 1499–1511.

Cerrato J. M., Ashner M. N., Alessi D. S., Lezama-Pacheco J. S., Bernier-Latmani R., Bargar J. R. and Giammar D. E. (2013) Relative Reactivity of Biogenic and Chemogenic Uraninite and Biogenic Noncrystalline U(IV). *Environ. Sci. Technol.* **47**, 9756–9763.

Chabaux F., Riotte J. and Dequincey O. (2003) U-Th-Ra Fractionation During Weathering and River Transport. *Rev. Mineral. Geochem.* **52**, 533–576.

Charlet L., Morin G., Rose J., Wang Y., Auffan M., Burnol A. and Fernandez-Martinez A. (2011) Reactivity at (nano)particle-water interfaces, redox processes, and arsenic transport in the environment. *Comptes Rendus Geosci.* **343**, 123–139.

Chen X., Zheng W. and Anbar A. D. (2020) Uranium Isotope Fractionation (238U/235U) during U(VI) Uptake by Freshwater Plankton. *Environ. Sci. Technol.* **54**, 2744–2752.

Cosmidis J., Benzerara K., Morin G., Busigny V., Lebeau O., Jézéquel D., Noël V., Dublet G. and Othmane G. (2014) Biomineralization of iron-phosphates in the water column of Lake Pavin (Massif Central, France). *Geochim. Cosmochim. Acta* **126**, 78–96.

Dang D. H., Novotnik B., Wang W., Georg R. B. and Evans R. D. (2016) Uranium Isotope Fractionation during Adsorption, (Co)precipitation, and Biotic Reduction. *Environ. Sci. Technol.* **50**, 12695–12704.

Denecke M. A., Reich T., Bubner M., Pompe S., Heise K. H., Nitsche H., Allen P. G., Bucher J. J., Edelstein N. M. and Shuh D. K. (1998) Determination of structural parameters of uranyl ions complexed with organic acids using EXAFS. *J. Alloys Compd.* **271–273**, 123–127.

Denecke M. A., Reich T., Pompe S., Bubner M., Heise K. H., Nitsche H., Allen P. G., Bucher J. J., Edelstein N. M. and Shun D. K. (1997) Differentiating Between Monodentate and Bidentate Carboxylate Ligands Coordinated to Uranyl Ions Using EXAFS. *J. Phys. IV* **7**, C2-637.

Dunham-Cheatham S., Rui X., Bunker B., Menguy N., Hellmann R. and Fein J. (2011) The effects of non-metabolizing bacterial cells on the precipitation of U, Pb and Ca phosphates. *Geochim. Cosmochim. Acta* **75**, 2828–2847.

Dusausoy Y., Ghermani N.-E., Podor R. and Cuney M. (1996) Low-temperature ordered phase of CaU (PO4) 2: synthesis and crystal structure. *Eur. J. Mineral.* **8**, 667–674.

Francis A. J. and Dodge C. J. (2008) Bioreduction of Uranium(VI) Complexed with Citric Acid by Clostridia Affects Its Structure and Solubility. *Environ. Sci. Technol.* **42**, 8277–8282.

Fuchs L. H. and Gebert E. (1958) X-ray studies of synthetic coffinite, thorite and uranothorites. *Am. Mineral.* **43**, 243–248.

Fuller A. J., Leary P., Gray N. D., Davies H. S., Mosselmans J. F. W., Cox F., Robinson C. H., Pittman J. K., McCann C. M., Muir M., Graham M. C., Utsunomiya S., Bower W. R., Morris K., Shaw S., Bots P., Livens F. R. and Law G. T. W. (2020) Organic complexation of U(VI) in reducing soils at a natural analogue site: Implications for uranium transport. *Chemosphere* **254**, 126859.

GEP (2010) *Recommandations pour la gestion des anciens sites miniers d'uranium en France. Des sites du Limousin aux autres sites, du court aux moyen et long termes.*, Groupe d'Expertise Pluraliste sur les sites miniers d'uranium du Limousin.

Gourgiotis A., Mangeret A., Manhès G., Blanchart P., Stetten L., Morin G., Le Pape P., Lefebvre P., Le Coz M. and Cazala C. (2020) New Insights into Pb Isotope Fingerprinting of U-Mine Material Dissemination in the Environment: Pb Isotopes as a Memory Dissemination Tracer. *Environ. Sci. Technol.* **54**, 797–806.

Guo L., Warnken K. W. and Santschi P. H. (2007) Retention behavior of dissolved uranium during ultrafiltration: Implications for colloidal U in surface waters. *Mar. Chem.* **107**, 156–166.

Howatson J., Grev D. M. and Morosin B. (1975) Crystal and molecular structure of uranyl acetate dihydrate. *J. Inorg. Nucl. Chem.* **37**, 1933–1935.

Ildefonse P., Cabaret D., Sainctavit P., Calas G., Flank A.-M. and Lagarde P. (1998) Aluminium X-ray absorption Near Edge Structure in model compounds and Earth's surface minerals. *Phys. Chem. Miner.* **25**, 112–121.

Ilton E. S., Haiduc A., Cahill C. L. and Felmy A. R. (2005) Mica Surfaces Stabilize Pentavalent Uranium. *Inorg. Chem.* **44**, 2986–2988.

Ilton E. S., Pacheco J. S. L., Bargar J. R., Shi Z., Liu J., Kovarik L., Engelhard M. H. and Felmy A. R. (2012) Reduction of U(VI) Incorporated in the Structure of Hematite. *Environ. Sci. Technol.* **46**, 9428–9436.

IRSN (2019) *MIMAUSA Database, Memory and Impact of uranium mines: synthesis and records.*, Institut de Radioprotection et de Sûreté Nucléaire.

Jemison N. E., Johnson T. M., Shiel A. E. and Lundstrom C. C. (2016) Uranium Isotopic Fractionation Induced by U(VI) Adsorption onto Common Aquifer Minerals. *Environ. Sci. Technol.* **50**, 12232–12240.

Kaplan D. I., Smith R., Parker C. J., Baker M., Cabrera T., Ferguson B. O., Kemner K. M., Laird M., Logan C., Lott J., Manglass L., Martinez N. E., Montgomery D., Seaman J. C., Shapiro M. and

Powell B. A. (2020) Uranium Attenuated by a Wetland 50 Years after Release into a Stream. *ACS Earth Space Chem.* **4**, 1360–1366.

Kelly S. D., Kemner K. M., Fein J. B., Fowle D. A., Boyanov M. I., Bunker B. A. and Yee N. (2002) X-ray absorption fine structure determination of pH-dependent U-bacterial cell wall interactions. *Geochim. Cosmochim. Acta* **66**, 3855–3871.

Krause M. O. and Oliver J. H. (1979) Natural widths of atomic K and L levels, Kα X-ray lines and several KLL Auger lines. *J. Phys. Chem. Ref. Data* **8**, 329–338.

Kubicki J. D., Halada G. P., Jha P. and Phillips B. L. (2009) Quantum mechanical calculation of aqueuous uranium complexes: carbonate, phosphate, organic and biomolecular species. *Chem. Cent. J.* **3**, 10.

Kvashnina K. O., Butorin S. M., Martin P. and Glatzel P. (2013) Chemical State of Complex Uranium Oxides. *Phys. Rev. Lett.* **111**, 253002.

Le Pape P., Stetten L., Hunault M. O. J. Y., Mangeret A., Brest J., Boulliard J.-C. and Morin G. (2020) HERFD-XANES spectroscopy at the U M4-edge applied to the analysis of U oxidation state in a heavily contaminated wetland soil. *Appl. Geochem.* **122**, 104714.

Lefebvre P., Gourgiotis A., Mangeret A., Sabatier P., Le Pape P., Diez O., Louvat P., Menguy N., Merrot P., Baya C., Zebracki M., Blanchart P., Malet E., Jézéquel D., Reyss J.-L., Bargar J. R., Gaillardet J., Cazala C. and Morin G. (2021a) Diagenetic formation of uranium-silica polymers in lake sediments over 3,300 years. *Proc. Natl. Acad. Sci.* **118**, e2021844118.

Lefebvre P., Noël V., Lau K. V., Jemison N. E., Weaver K. L., Williams K. H., Bargar J. R. and Maher K. (2019) Isotopic Fingerprint of Uranium Accumulation and Redox Cycling in Floodplains of the Upper Colorado River Basin. *Environ. Sci. Technol.* **53**, 3399–3409.

Lefebvre P., Sabatier P., Mangeret A., Gourgiotis A., Le Pape P., Develle A.-L., Louvat P., Diez O., Reyss J.-L., Gaillardet J., Cazala C. and Morin G. (2021b) Climate-driven fluxes of organic-bound uranium to an alpine lake over the Holocene. *Sci. Total Environ.* **783**, 146878.

Li D., Kaplan D. I., Chang H.-S., Seaman J. C., Jaffé P. R., Koster van Groos P., Scheckel K. G., Segre C. U., Chen N., Jiang D.-T., Newville M. and Lanzirotti A. (2015) Spectroscopic Evidence of Uranium Immobilization in Acidic Wetlands by Natural Organic Matter and Plant Roots. *Environ. Sci. Technol.* **49**, 2823–2832.

Llorens I., Untereiner G., Jaillard D., Gouget B., Chapon V. and Carriere M. (2012) Uranium Interaction with Two Multi-Resistant Environmental Bacteria: Cupriavidus metallidurans CH34 and Rhodopseudomonas palustris. *PLOS ONE* **7**, e51783.

Locock A. J. and Burns P. C. (2003) Crystal structures and synthesis of the copper-dominant members of the autunite and meta-autunite groups: torbernite, zeunerite, metatorbernite and metazeunerite. *Can. Mineral.* **41**, 489–502.

Maher K., Bargar J. R. and Brown G. E. (2013) Environmental Speciation of Actinides. *Inorg. Chem.* **52**, 3510–3532.

Maillot F., Morin G., Wang Y., Bonnin D., Ildefonse P., Chaneac C. and Calas G. (2011) New insight into the structure of nanocrystalline ferrihydrite: EXAFS evidence for tetrahedrally coordinated iron(III). *Geochim. Cosmochim. Acta* **75**, 2708–2720.

Malinowski E. R. (1977) Determination of the number of factors and the experimental error in a data matrix. *Anal. Chem.* **49**, 612–617.

Mangeret A., Blanchart P., Alcalde G., Amet X., Cazala C. and Gallerand M.-O. (2018) An evidence of chemically and physically mediated migration of 238U and its daughter isotopes in the vicinity of a former uranium mine. *J. Environ. Radioact.* **195**, 67–71.

Martin A., Hassan-Loni Y., Fichtner A., Péron O., David K., Chardon P., Larrue S., Gourgiotis A., Sachs S., Arnold T., Grambow B., Stumpf T. and Montavon G. (2020) An integrated approach combining soil profile, records and tree ring analysis to identify the origin of environmental contamination in a former uranium mine (Rophin, France). *Sci. Total Environ.* **747**, 141295.

Merrot P., Juillot F., Noël V., Lefebvre P., Brest J., Menguy N., Guigner J.-M., Blondeau M., Viollier E., Fernandez J.-M., Moreton B., Bargar J. R. and Morin G. (2019) Nickel and iron partitioning between clay minerals, Fe-oxides and Fe-sulfides in lagoon sediments from New Caledonia. *Sci. Total Environ.* **689**, 1212–1227.

Merroun M. L., Raff J., Rossberg A., Hennig C., Reich T. and Selenska-Pobell S. (2005) Complexation of Uranium by Cells and S-Layer Sheets of Bacillus sphaericus JG-A12. *Appl. Environ. Microbiol.* **71**, 5532–5543.

Meyers P. A. and Teranes J. L. (2001) Sediment Organic Matter. In *Tracking Environmental Change Using Lake Sediments: Physical and Geochemical Methods* (eds. W. M. Last and J. P. Smol). Developments in Paleoenvironmental Research. Springer Netherlands, Dordrecht. pp. 239–269.

Mikutta C., Langner P., Bargar J. R. and Kretzschmar R. (2016) Tetra- and Hexavalent Uranium Forms Bidentate-Mononuclear Complexes with Particulate Organic Matter in a Naturally Uranium-Enriched Peatland. *Environ. Sci. Technol.* **50**, 10465–10475.

Morin G., Mangeret A., Othmane G., Stetten L., Seder-Colomina M., Brest J., Ona-Nguema G., Bassot S., Courbet C. and Guillevic J. (2016) Mononuclear U(IV) complexes and ningyoite as major uranium species in lake sediments. *Geochem. Perspect. Lett.* **2**, 95–105.

Muñoz M., Argoul P. and Farges F. (2003) Continuous Cauchy wavelet transform analyses of EXAFS spectra: A qualitative approach. *Am. Mineral.* **88**, 694–700.

Muñoz M., Farges F. and Argoul P. (2005) Continuous Cauchy wavelet transform of XAFS spectra. *Phys. Scr.* **2005**, 221.

Newsome L., Morris K. and Lloyd J. R. (2014) The biogeochemistry and bioremediation of uranium and other priority radionuclides. *Chem. Geol.* **363**, 164–184.

Newsome L., Morris K., Shaw S., Trivedi D. and Lloyd J. R. (2015) The stability of microbially reduced U(IV); impact of residual electron donor and sediment ageing. *Chem. Geol.* **409**, 125–135.

Noël V., Boye K., Kukkadapu R. K., Li Q. and Bargar J. R. (2019) Uranium storage mechanisms in wet-dry redox cycled sediments. *Water Res.* **152**, 251–263.

Noël V., Boye K., Lezama Pacheco J. S., Bone S. E., Janot N., Cardarelli E., Williams K. H. and Bargar J. R. (2017) Redox Controls over the Stability of U(IV) in Floodplains of the Upper Colorado River Basin. *Environ. Sci. Technol.* **51**, 10954–10964.

Othmane G., Allard T., Morin G., Sélo M., Brest J., Llorens I., Chen N., Bargar J. R., Fayek M. and Calas G. (2013) Uranium Association with Iron-Bearing Phases in Mill Tailings from Gunnar, Canada. *Environ. Sci. Technol.* **47**, 12695–12702.

Owen D. E. and Otton J. K. (1995) Mountain wetlands: Efficient uranium filters — potential impacts. *Ecol. Eng.* **5**, 77–93.

Palmer M. R. and Edmond J. M. (1993) Uranium in river water. *Geochim. Cosmochim. Acta* **57**, 4947–4955.

Pidchenko I., Kvashnina K. O., Yokosawa T., Finck N., Bahl S., Schild D., Polly R., Bohnert E., Rossberg A., Göttlicher J., Dardenne K., Rothe J., Schäfer T., Geckeis H. and Vitova T. (2017) Uranium Redox Transformations after U(VI) Coprecipitation with Magnetite Nanoparticles. *Environ. Sci. Technol.* **51**, 2217–2225.

Ravel B. and Newville M. (2005) ATHENA, ARTEMIS, HEPHAESTUS: data analysis for X-ray absorption spectroscopy using IFEFFIT. *J. Synchrotron Radiat.* **12**, 537–541.

Regenspurg S., Margot-Roquier C., Harfouche M., Froidevaux P., Steinmann P., Junier P. and Bernier-Latmani R. (2010) Speciation of naturally-accumulated uranium in an organic-rich soil of an alpine region (Switzerland). *Geochim. Cosmochim. Acta* **74**, 2082–2098.

Rossberg A., Ulrich K.-U., Weiss S., Tsushima S., Hiemstra T. and Scheinost A. C. (2009) Identification of Uranyl Surface Complexes on Ferrihydrite: Advanced EXAFS Data Analysis and CD-MUSIC Modeling. *Environ. Sci. Technol.* **43**, 1400–1406.

Rudnick R. L. and Gao S. (2003) Composition of the continental crust. In *The crust* (eds. H. D. Holland, K. K. Turekian, and R. L. Rudnick). Treatise on Geochemistry. Elsevier, Amsterdam. pp. 1–64.

Rui X., Kwon M. J., O'Loughlin E. J., Dunham-Cheatham S., Fein J. B., Bunker B., Kemner K. M. and Boyanov M. I. (2013) Bioreduction of Hydrogen Uranyl Phosphate: Mechanisms and U(IV) Products. *Environ. Sci. Technol.* **47**, 5668–5678.

Russell W. A., Papanastassiou D. A. and Tombrello T. A. (1978) Ca isotope fractionation on the Earth and other solar system materials. *Geochim. Cosmochim. Acta* **42**, 1075–1090.

Schlosser F., Krüger S. and Rösch N. (2006) A Density Functional Study of Uranyl Monocarboxylates. *Inorg. Chem.* **45**, 1480–1490.

Schmeide K., Sachs S., Bubner M., Reich T., Heise K. H. and Bernhard G. (2003) Interaction of uranium(VI) with various modified and unmodified natural and synthetic humic substances studied by EXAFS and FTIR spectroscopy. *Inorganica Chim. Acta* **351**, 133–140.

Schöner A., Noubactep C., Büchel G. and Sauter M. (2009) Geochemistry of natural wetlands in former uranium milling sites (eastern Germany) and implications for uranium retention. *Geochemistry* **69**, 91–107.

Schumann R. R., Zielinski R. A., Otton J. K., Pantea M. P. and Orem W. H. (2017) Uranium delivery and uptake in a montane wetland, north-central Colorado, USA. Appl. Geochem. 78, 363–379.

Seder-Colomina M., Mangeret A., Stetten L., Merrot P., Diez O., Julien A., Barker E., Thouvenot A., Bargar J., Cazala C. and Morin G. (2018) Carbonate Facilitated Mobilization of Uranium from Lacustrine Sediments under Anoxic Conditions. *Environ. Sci. Technol.* **52**, 9615–9624.

Seder-Colomina M., Morin G., Brest J., Ona-Nguema G., Gordien N., Pernelle J.-J., Banerjee D., Mathon O., Esposito G. and van Hullebusch E. D. (2015) Uranium(VI) Scavenging by Amorphous Iron Phosphate Encrusting Sphaerotilus natans Filaments. *Environ. Sci. Technol.* **49**, 14065–14075.

Shiel A. E., Laubach P. G., Johnson T. M., Lundstrom C. C., Long P. E. and Williams K. H. (2013) No Measurable Changes in 238U/235U due to Desorption–Adsorption of U(VI) from Groundwater at the Rifle, Colorado, Integrated Field Research Challenge Site. *Environ. Sci. Technol.* **47**, 2535–2541.

Solé V. A., Papillon E., Cotte M., Walter Ph. and Susini J. (2007) A multiplatform code for the analysis of energy-dispersive X-ray fluorescence spectra. *Spectrochim. Acta Part B At. Spectrosc.* **62**, 63–68.

Stetten L., Blanchart P., Mangeret A., Lefebvre P., Le Pape P., Brest J., Merrot P., Julien A., Proux O., Webb S. M., Bargar J. R., Cazala C. and Morin G. (2018a) Redox Fluctuations and Organic Complexation Govern Uranium Redistribution from U(IV)-Phosphate Minerals in a Mining-Polluted Wetland Soil, Brittany, France. *Environ. Sci. Technol.* **52**, 13099–13109.

Stetten L., Lefebvre P., Le Pape P., Mangeret A., Blanchart P., Merrot P., Brest J., Julien A., Bargar J. R., Cazala C. and Morin G. (2020) Experimental redox transformations of uranium phosphate minerals and mononuclear species in a contaminated wetland. *J. Hazard. Mater.* **384**, 121362.

Stetten L., Mangeret A., Brest J., Seder-Colomina M., Le Pape P., Ikogou M., Zeyen N., Thouvenot A., Julien A., Alcalde G., Reyss J. L., Bombled B., Rabouille C., Olivi L., Proux O., Cazala C. and Morin G. (2018b) Geochemical control on the reduction of U(VI) to mononuclear U(IV) species in lacustrine sediments. *Geochim. Cosmochim. Acta* **222**, 171–186.

Stirling C. H., Andersen M. B., Warthmann R. and Halliday A. N. (2015) Isotope fractionation of 238U and 235U during biologically-mediated uranium reduction. *Geochim. Cosmochim. Acta* **163**, 200–218.

Stylo M., Neubert N., Wang Y., Monga N., Romaniello S. J., Weyer S. and Bernier-Latmani R. (2015) Uranium isotopes fingerprint biotic reduction. *Proc. Natl. Acad. Sci.* **112**, 5619–5624.

Teo B. K. (1986) *EXAFS: Basic Principles and Data Analysis.*, Springer, Berlin, Heidelberg.

Thompson H. A., Brown G. E. and Parks G. A. (1997) XAFS spectroscopic study of uranyl coordination in solids and aqueous solution. *Am. Mineral.* **82**, 483–496.

Wang Y., Bagnoud A., Suvorova E., McGivney E., Chesaux L., Phrommavanh V., Descostes M. and Bernier-Latmani R. (2014) Geochemical Control on Uranium(IV) Mobility in a Mining-Impacted Wetland. *Environ. Sci. Technol.* **48**, 10062–10070.

Wang Y., Frutschi M., Suvorova E., Phrommavanh V., Descostes M., Osman A. A. A., Geipel G. and Bernier-Latmani R. (2013) Mobile uranium(IV)-bearing colloids in a mining-impacted wetland. *Nat. Commun.* **4**, 1–9.

Wang Y., Morin G., Ona-Nguema G., Juillot F., Calas G. and Brown G. E. (2011) Distinctive Arsenic(V) Trapping Modes by Magnetite Nanoparticles Induced by Different Sorption Processes. *Environ. Sci. Technol.* **45**, 7258–7266.

Webb S. M. (2005) SIXpack: a graphical user interface for XAS analysis using IFEFFIT. *Phys. Scr.* **2005**, 1011.

Zeyen N., Benzerara K., Menguy N., Brest J., Templeton A. S., Webb S. M., Gérard E., Moreira D., López-García P., Tavera R. and Morin G. (2019) Fe-bearing phases in modern lacustrine microbialites from Mexico. *Geochim. Cosmochim. Acta* **253**, 201–230.